

1 **Microseismic Constraints on the Mechanical State of**
2 **the North Anatolian Fault Zone Thirteen Years after**
3 **the 1999 M7.4 Izmit Earthquake**

4 **Eric Beaucé^{1,3}, Robert D. van der Hilst¹, Michel Campillo^{2,1}**

5 ¹Department of Earth, Atmospheric, and Planetary Sciences, Massachusetts Institute of Technology, USA

6 ²Institut des Sciences de la Terre, Université Grenoble Alpes, France

7 ³Lamont-Doherty Earth Observatory, Columbia University, NY, USA

8 **Key Points:**

- 9 • We built an extensive earthquake catalog using our new automated method along
10 the western NAFZ.
- 11 • We observe variable statistical properties, b-value, and temporal clustering along
12 the fault.
- 13 • The properties of the Sapanca seismicity support the possibility of slow slip in the
14 step-over.

Corresponding author: Eric Beaucé, ebeauce@ldeo.columbia.edu

Abstract

The 17 August 1999 M_w 7.4 Izmit earthquake ruptured the western section of the North Anatolian Fault Zone (NAFZ) and strongly altered the fault zone properties and stress field. Consequences of the co- and post-seismic stress changes were seen in the spatio-temporal evolution of the seismicity and in the surface slip rates. Thirteen years after the Izmit earthquake, in 2012, the dense seismic array DANA was deployed for 1.5 years. We built a new catalog of microseismicity ($M < 2$) by applying our automated detection and location method to the DANA data set. Our method combines a systematic backprojection of the seismic wavefield and template matching. We analyzed the statistical properties of the catalog by computing the Gutenberg-Richter b-value and by quantifying the amount of temporal clustering in groups of nearby earthquakes. We found that the microseismicity mainly occurs off the main fault and that the most active regions are the Lake Sapanca step-over and near the Akyazi fault. Based on previous studies, we interpreted the b-values and temporal clustering *i*) as indicating that the Akyazi seismicity is occurring in high background stresses and is driven by the Izmit earthquake residual stresses, and *ii*) as suggesting evidence that intricate seismic and aseismic slip was taking place on heterogeneous faults at the eastern Lake Sapanca, near the brittle-ductile transition. Geodesy shows enhanced north-south extension around Lake Sapanca following the Izmit earthquake, therefore, the seismicity supports the possibility of slow slip at depth in the step-over.

Plain Language Summary

On 17 August 1999, a large M7.4 earthquake struck near the city of Izmit, in western Turkey, and caused important human and material losses. The earthquake resulted from the large and sudden displacement of crustal blocks along the North Anatolian Fault Zone (NAFZ). Transient changes in the crustal and fault properties are commonly observed following such large events. In this study, we analyzed the statistical properties of microearthquakes, that is, of small earthquakes ($M < 2$) typically too small to affect the surrounding population, to gain knowledge about the state of the NAF more than a decade after the Izmit earthquake. First, we addressed the challenge of locating microearthquakes, in space and time, by applying our automatic earthquake detection and location algorithm. Then, the statistical analysis allowed us to characterize physical properties of the NAF and, thus, to highlight the peculiar properties of faults near Lake Sapanca. We interpreted that these faults are heterogeneous and slip both seismically and aseismically. Our study calls for taking a closer look at the extension across Lake Sapanca with different, complementary geophysical methods.

1 Introduction

The North Anatolian Fault Zone (NAFZ) is a 1,500 km long strike-slip fault that marks the boundary between the Anatolian plate in the south and the Eurasian plate in the north (Figure 1A). The fault slips, overall, in a right-lateral manner to accommodate the westward motion of Anatolia with respect to Eurasia due to the combination of the subduction along the Hellenic trench and the Cyprus trench in the southwest and the south and the collision with Arabia in the southeast (Le Pichon & Angelier, 1979; McClusky et al., 2000; Reilinger et al., 2006). Near the Gulf of Izmit, in western Turkey, the NAFZ splits into a northern strand and a southern strand. These two strands bound the Almacik mountains in the east and the Armutlu block in the west, and separate the Istanbul Zone in the north from the Sakarya Terrane in the south, which are the remains of the passive margin of the Intra-Pontide Ocean (see Figure 1B, *e.g.* Akbayram et al., 2013). Most of the deformation is accommodated on the northern strand (*e.g.* Meade et al., 2002; Reilinger et al., 2006).

64 The 17 August 1999 M7.4 Izmit earthquake and the 12 November 1999 Düzce M7.2
65 earthquake are the most recent (as of the time of writing) events of a series of westward
66 migrating $M > 7$ earthquakes that ruptured almost entirely the North Anatolian Fault
67 Zone (*e.g.* Toksöz et al., 1979; Stein et al., 1997). The Izmit earthquake nucleated near
68 the Izmit Bay, propagated bilaterally and broke a 150 km-long, almost vertical section
69 of the fault made of four, or five, segments along the northern strand (Toksoz et al., 1999;
70 Barka et al., 2002). To the east, the rupture propagated at super-shear speeds (Bouchon
71 et al., 2001, 2011) and broke the Izmit-Sapanca, the Sapanca-Akyazi and the Karadere
72 segments (*cf.* names on Figure 1B). To the west, the rupture propagated along the Gölcük
73 segment and stopped on the Yalova segment (Langridge et al., 2002), increasing the prob-
74 ability of major failure further west beneath the Marmara Sea (Parsons et al., 2000). The
75 Düzce earthquake nucleated near the eastern termination of the Izmit earthquake, likely
76 due to increased Coulomb stress (Parsons et al., 2000; Utkucu et al., 2003). The co- and
77 post-seismic stress changes and the transient changes of the fault’s mechanical proper-
78 ties caused by the Izmit earthquake affected the local seismicity patterns and the focal
79 mechanisms of microearthquakes (*e.g.* Bohnhoff et al., 2006; Pınar et al., 2010; Ickrath
80 et al., 2015). GPS and interferometric synthetic aperture radar (InSAR) observations
81 suggest that fast and rapidly decaying deep afterslip occurred in the middle-to-lower crust
82 in the months following the Izmit-Düzce earthquake sequence (*e.g.* Reilinger et al., 2000;
83 Bürgmann et al., 2002), then relayed by slower post-seismic slip at depth (Ergintav et
84 al., 2009; Hearn et al., 2009). Patterns of surface displacement also suggest the existence
85 of shallow creep along the Izmit-Sapanca and the Sapanca-Akyazi segments (*e.g.* Çakir
86 et al., 2012; Hussain et al., 2016). Transient creep episodes have been identified more than
87 a decade after the Izmit earthquake (Aslan et al., 2019).

88 Despite the overall good understanding of the east-west motion along the western
89 NAFZ, smaller scale, north-south extension at some locations remains enigmatic. Co-
90 and post-seismic slip on vertical fault segments seems unable to reproduce the patterns
91 of north-south extension observed in geodetic data (*e.g.* Ergintav et al., 2009; Hearn et
92 al., 2009). Even though refining the geometry of the main fault segments of the NAFZ
93 helps explain the observations (*e.g.* slightly north dipping faults, Çakir et al., 2003), mod-
94 els of the post- and inter-seismic deformation along the NAFZ would benefit from tak-
95 ing into account secondary structures, such as the faults in step-overs. Microseismicity
96 ($M < 2$) provides information at small length scales at seismogenic depths and thus is
97 complimentary to geodetic data in building a better understanding of slip along the NAFZ
98 (aseismic vs seismic, distributed vs localized), that is, of its mechanical state.

99 The abundant number of microearthquakes makes them well-suited for statistical
100 analyses. Of interest to this study are the b -value of the Gutenberg-Richter law (Gutenberg
101 & Richter, 1941) that describes the frequency-magnitude distribution of a population
102 of earthquakes, and the fractal dimension D of the earthquake occurrence time series (Smalley Jr
103 et al., 1987; Beaucé et al., 2019) that quantifies the strength of temporal clustering. The
104 b -value acts as a stressmeter (Amelung & King, 1997; C. H. Scholz, 2015), and the frac-
105 tal dimension D is related to the density of fractures and seismic-aseismic slip partition-
106 ing (C. Scholz, 1968; Dublanchet et al., 2013).

107 The dense seismic array DANA (Dense Array for North Anatolia DANA, 2012,
108 see Figure 1C) was deployed around the rupture trace of the 1999-08-17 Izmit earthquake,
109 it operated about thirteen years later from early May 2012 to late September 2013. These
110 data enabled multiple studies that improved our understanding of the complex struc-
111 tures and seismicity patterns in the region (*e.g.* Poyraz et al., 2015; Kahraman et al.,
112 2015; Papaleo et al., 2018; Taylor et al., 2019). Here, we study microearthquakes in or-
113 der to improve our understanding of the mechanical state of the North Anatolian Fault
114 Zone more than a decade after the 1999 M7.4 Izmit earthquake. First, we briefly describe
115 our automated earthquake detection and location method (Section 2), and then present
116 the earthquake catalog (Section 3.1) and a statistical analysis of collective properties of
117 earthquakes (b -value, Section 3.2, and temporal clustering, Section 3.3). These obser-
118 vations allow a characterization of the physical environment in which seismicity takes

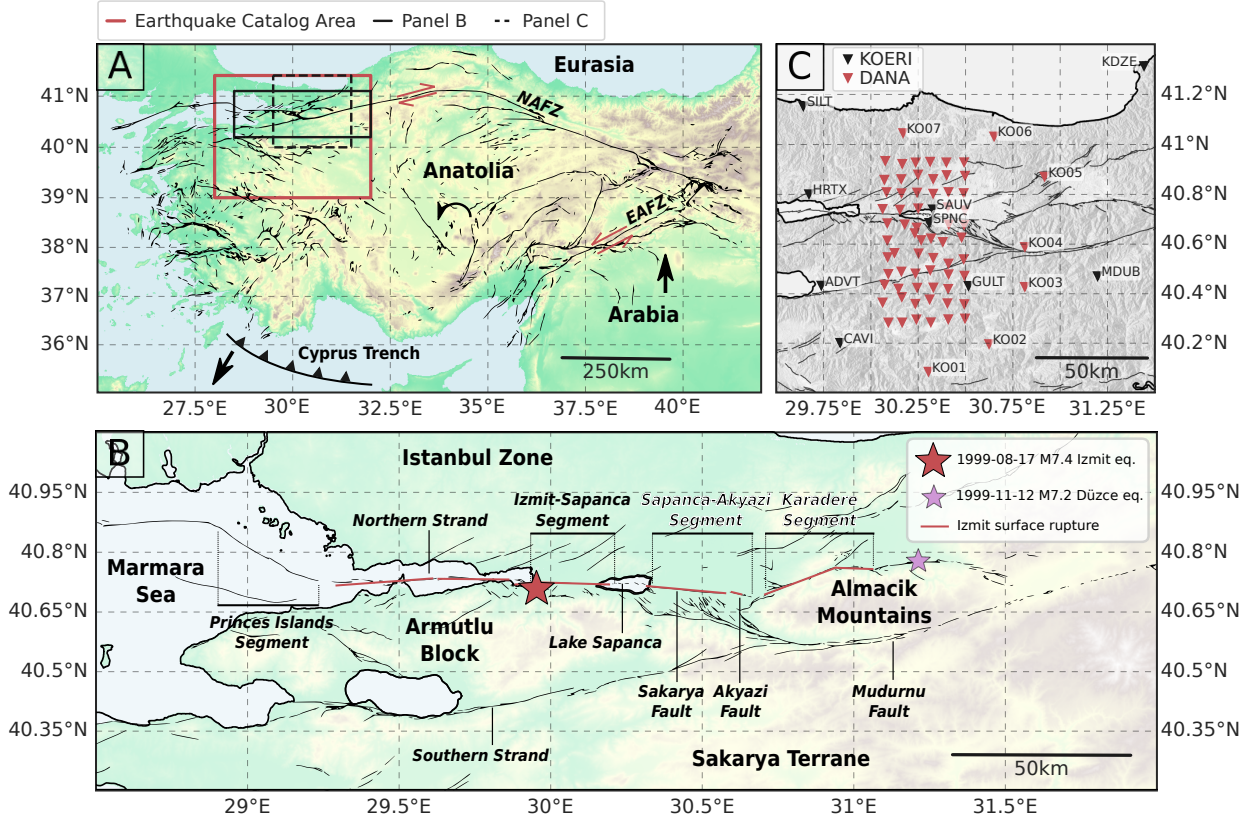


Figure 1. **A:** Large scale view of the North Anatolian Fault Zone. Abbreviations: NAFZ - North Anatolian Fault Zone, EAFZ - East Anatolian Fault Zone. The red arrows indicate the direction of coseismic motion. Our study region is located at the western end of the NAFZ. **B:** Magnified view of the fault zone in our study region. Larger font names are the main geologic units: Istanbul Zone, Armutlu Block, Almacik Mountains and Sakarya Terrane. The smaller font, italic names are segments and faults of the NAFZ: the Izmit-Sapanca segment, the Sapanca lake step-over, the Sapanca-Akyazi segment (which together constitute the northern strand), the Karadere segment and the southern strand (names following Barka et al., 2002). The Sapanca-Akyazi segment is made of the Sakarya fault and the Akyazi fault. The flat area around the Akyazi fault is referred to as the Akyazi plain. Both Lake Sapanca and the Akyazi plain are pull-apart basins. The large red star indicates the epicenter of the M_w 7.4 Izmit earthquake, and the small purple star indicates the epicenter of the M_w 7.2 Düzce earthquake. **C:** The seismic stations used in this study are from the temporary experiment DANA (70 stations, red triangles; DANA, 2012) and the permanent network (9 stations, black triangles; Kandilli Observatory And Earthquake Research Institute, Boğaziçi University, 1971). Each column of the DANA array is indexed by a letter and each row is indexed by a number (DA01, DA02, ..., DB01, ...).

119 place. We interpret and discuss our results to question the role of secondary structures
 120 in the dynamics of NAFZ (Section 4).

2 Methodology

2.1 Data

The continuous seismic data were recorded by broadband stations from the temporary array DANA (70 stations) and the permanent network KOERI (9 stations, see the locations in Figure 1, and the Data and Resources section). The time period covered by this study is set by the duration of the DANA experiment: 2012-05-04 to 2013-09-20. Sampling rates are 50 Hz for all stations but SAUV, which samples at 100 Hz. We bandpass filtered the data between 2 Hz and 12 Hz to eliminate low frequency noise and to allow us to downsample the time series to 25 Hz in order to make the computation less intensive.

2.2 Earthquake Detection, Location, and Magnitude Estimation

We analyzed the 2012-05-04/2013-09-20 time period with a fully automatized earthquake detection and location method. The core of the workflow, summarized in Figure 2, consists of three stages:

1. Backprojection (Section 2.2.1): The energy of the seismic wavefield is continuously backprojected onto a 3D grid of potential sources to detect coherent (earthquake) sources.
2. Relocation (Section 2.2.2): The P- and S-wave first arrivals of the previously detected events are identified with the automatic phase picker PhaseNet (Zhu & Beroza, 2019), and the picks are used in the NonLinLoc earthquake location software (Lomax et al., 2000, 2009).
3. Template matching (Section 2.2.3): The successfully relocated earthquakes are used as template earthquakes in a matched-filter search to detect other, smaller earthquakes in the same region using the Fast Matched Filter software (Beaucé et al., 2018).

The detection method is discussed in detail in Beaucé et al. (2019), but the relocation is now fully automated and includes PhaseNet and NonLinLoc. In an extra step, we further characterized the detected earthquakes by relocating them with the double-difference method (Section 2.2.4) and estimating their magnitude (Section 2.2.5).

2.2.1 Backprojection and Location

We continuously backprojected the energy of the seismic wavefield recorded at the array of seismic stations onto a 3D grid of potential sources beneath the study region, searching for the space-time locations of coherent sources. Backprojection is now a widely used earthquake detection and source imaging method (*e.g.* Ishii et al., 2005; Walker et al., 2005; Honda & Aoi, 2009; W. Frank & Shapiro, 2014). We computed the composite network response (CNR):

$$\text{CNR}(t) = \max_k \{\text{NR}_k(t)\}; \quad \text{NR}_k(t) = \sum_{s,c} \text{env} \left(u_{s,c}(t + \tau_{s,c}^{(k)}) \right). \quad (1)$$

In this equation, t is the detection time and $\text{NR}_k(t)$ is the network response for source location indexed by k at time t . $\text{NR}_k(t)$ is the sum of the envelopes (the modulus of the analytical signal) of the seismograms $u_{s,c}$ shifted in time by the moveout $\tau_{s,c}^{(k)}$ on station s and component c . The moveouts were computed using the ray-tracing software Pykonal (White et al., 2020) in the 1D velocity model from Karabulut et al. (2011) (see Table S1). We note that the use of a 1D velocity model in this region can introduce significant errors in the earthquake locations because of the strong lateral velocity variations, in particular across the two strands of the NAFZ (*e.g.* Karahan et al., 2001; Kahraman et al., 2015; Papaleo et al., 2018). This velocity model produced a visually satisfying agreement between earthquake epicenters and fault surface traces, and allowed consistency with a

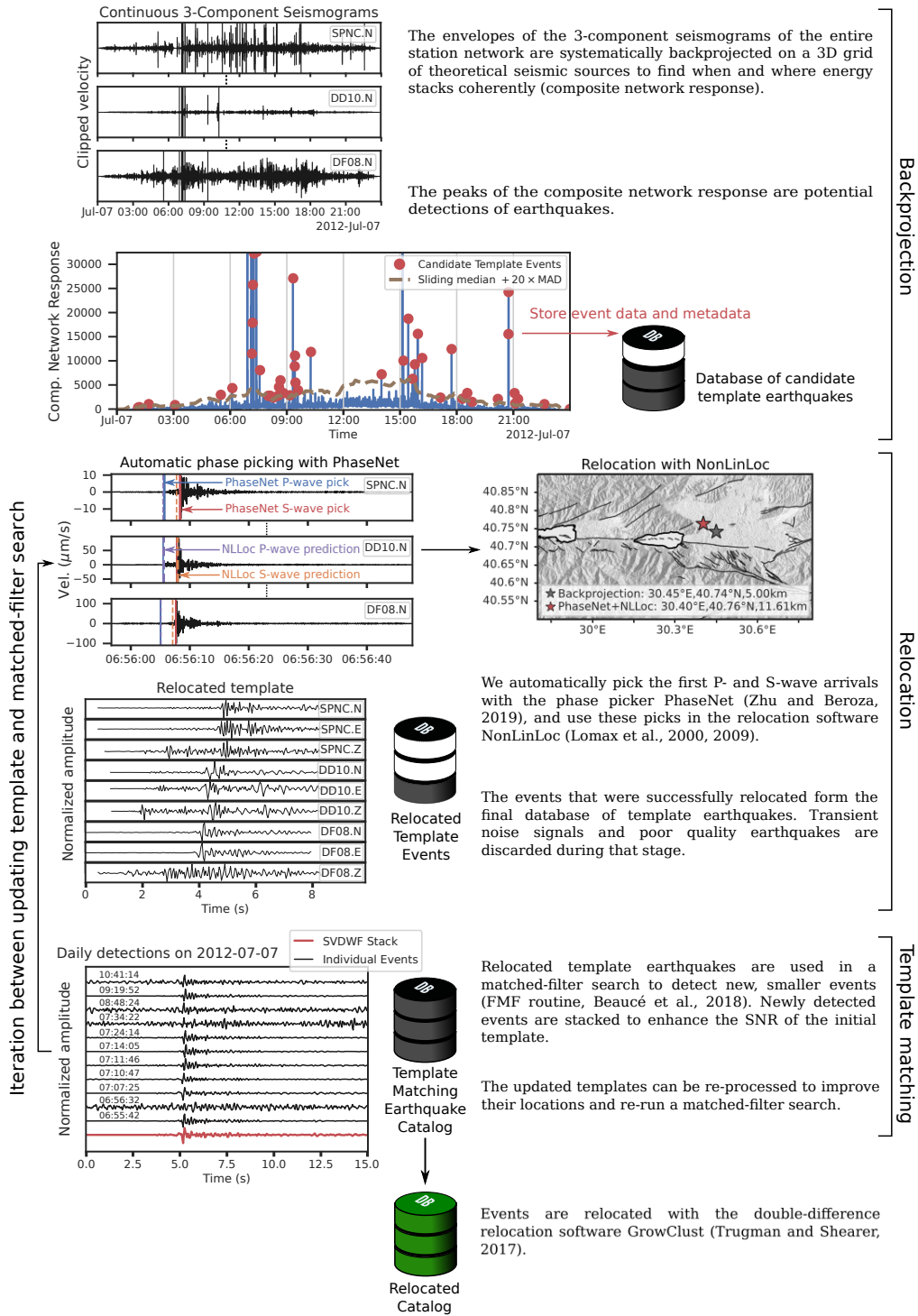


Figure 2. Summary flowchart of the earthquake detection and location method. For clarity, only a subset of stations are shown in the above panels, but all the analysis is carried on the 79 stations together. Template matching is performed on the 10 stations closest to the source and the detection threshold is set to $8 \times \text{RMS}$ of the correlation coefficients in a 30-minute sliding window. See Data and Resources for code availability.

168 previous study on the same data set (Poyraz et al., 2015). The backprojection method
 169 naturally provides an estimate of the location of each detected events. However, the net-
 170 work response finds the times that aligned the envelope maxima rather than the P- and
 171 S-wave arrivals, which results in approximate locations.

172 **2.2.2 Relocation**

173 All the events detected through the CNR were processed with the deep neural net-
 174 work PhaseNet (Zhu & Beroza, 2019) to automatically pick the P- and S-wave first ar-
 175 rivals. These picks were then used by the location software NonLinLoc (Lomax et al.,
 176 2000, 2009) to get the earthquake locations and their uncertainties given as 1- σ inter-
 177 vals. We required at least four P- and S-wave picks and a total minimum of 15 picks to
 178 relocate an event. Requiring both P- and S-wave picks helps constrain the earthquake
 179 depth, and imposing at least 15 picks efficiently reduced the number of solutions with
 180 very large uncertainties. Events that could not be successfully relocated with NonLin-
 181 Loc (*e.g.* noisy picks, multiple sources recorded at the same time) were discarded. More
 182 information about the input parameters used by PhaseNet and NonLinLoc can be found
 183 in Supplementary Material (Section 1).

184 **2.2.3 Template Matching**

185 Successfully relocated events were kept as templates and used in a matched-filter
 186 search to detect new, smaller magnitude earthquakes. Template matching is a power-
 187 ful method for detecting low signal-to-noise ratio (SNR) events given prior knowledge
 188 of the target seismicity (*e.g.* Gibbons & Ringdal, 2006; Shelly et al., 2007; Ross et al.,
 189 2019). It consists in searching for all earthquakes with similar waveforms and moveouts
 190 to a known earthquake, that is, earthquakes sharing a similar location and focal mech-
 191 anism. The similarity is measured by the network-averaged correlation coefficient (CC)
 192 between the template waveforms $T_{s,c}$ and the seismograms $u_{s,c}$ shifted by the template
 193 moveout $\tau_{s,c}$:

$$194 \quad \text{CC}(t) = \sum_{s,c} w_{s,c} \sum_{n=1}^N \frac{T_{s,c}(t_n)u_{s,c}(t+t_n+\tau_{s,c})}{\sqrt{\sum_{n=1}^N T_{s,c}^2(t_n) \sum_{n=1}^N u_{s,c}^2(t+t_n+\tau_{s,c})}}, \quad (2)$$

195 where $w_{s,c}$ is the weight attributed to station s , component c , and N is the length of the
 196 template waveforms. We ran the matched-filter search on multiple nodes of a super-computer
 197 equipped with Graphic Processing Units (GPUs) using the template matching software
 198 Fast Matched Filter (Beaucé et al., 2018). We used a template window of 8 seconds start-
 199 ing 4 seconds before the S wave on the horizontal components and 1 second before the
 200 P wave on the vertical components. We used a detection threshold of 8 times the root
 201 mean square (RMS) of the CC time series in a 30-minute sliding window ($8 \times \text{RMS}\{\text{CC}(t)\}$).
 202 The 8 s template duration is adequate given the signal duration of small magnitude earth-
 203 quakes at ~ 10 -50 km source-receiver distances. The $8 \times \text{RMS}$ threshold is in the con-
 204 servative range of commonly used threshold in template matching studies (*e.g.* Shelly
 205 et al., 2007; Ross et al., 2019). Note that $8 \times \text{RMS}$ is about 12 times the median ab-
 206 solute deviation (MAD) for a gaussian distribution.

207 After a matched-filter search over the whole study period, each template earthquake
 208 has detected potentially many new similar earthquakes. The similarity of the detected
 209 events can be leveraged to form higher SNR waveforms of the template earthquake by
 210 summing them. We used the Singular Value Decomposition and Wiener Filtering method
 211 (Moreau et al., 2017) for the efficient extraction of coherent signal in the recordings of
 212 similar earthquakes. The new template earthquakes with higher SNR waveforms were
 213 in turn used to refine the locations, and run another iteration of the matched-filter search.
 214 This detection/stacking/relocation workflow is commonly iterated several times in tem-
 215 plate matching studies. However, stacking the waveforms of similar earthquakes cancels
 216 out their differences at high frequencies, and thus acts as a low-pass filter that removes

217 the short-scale information contained in the exact location of an individual event. In or-
 218 der to trade-off the SNR improvement with the loss of short-scale information, we iter-
 219 ated only once in this study.

220 Neighboring templates often detect the same events, therefore we kept a single event
 221 out of all detections occurring within three seconds of each other, from templates whose
 222 uncertainty ellipsoids were separated by less than 5 km, and with average waveform sim-
 223 ilarity greater than 0.33. These thresholds were chosen based on physical considerations
 224 (the time threshold 3 sec assumes location errors of up to 10-15 km, the space threshold
 225 5 km accounts for coherency of waves at 2 Hz, etc) and empirically by inspecting the out-
 226 put catalog for duplicated events.

227 **2.2.4 Double-Difference Relative Relocation**

228 We refined the earthquake locations in the region of interest, near the NAFZ and
 229 beneath the stations, with the double-difference relative relocation method (*e.g.* Poupinet
 230 et al., 1984; Waldhauser & Ellsworth, 2000). P- and S-wave differential arrival times were
 231 computed by finding the lag times that maximize the inter-event correlation coefficients
 232 and summing them to the travel time differences. The differential times were then pro-
 233 cessed by the relocation software GrowClust (Trugman & Shearer, 2017, additional in-
 234 formation on parameters are given in Supplementary Material). GrowClust estimates
 235 location uncertainties with the non-parametric bootstrap resampling method (Efron &
 236 Tibshirani, 1986). The original data set is perturbed multiple times by randomly sam-
 237 pling the differential travel times and repeating the location procedure on each such repli-
 238 cated data set. Variations in the locations thus obtained give the position errors.

239 **2.2.5 Magnitude Estimation**

240 Local magnitudes were computed from the amplitude ratios of peak velocities. This
 241 required estimating the magnitude of at least one event per template to calibrate our
 242 local magnitude scale. Therefore, we computed the moment magnitude M_w by fitting
 243 the Brune model (Equation (3), Brune, 1970) to the multi-station average displacement
 244 spectra that satisfied an SNR criterion (see details in Section 1.6 and Figure S1).

$$245 \quad |u_{\text{Brune}}(f)| = \frac{\Omega_0}{\left(1 + \frac{f}{f_c}\right)^2}. \quad (3)$$

246 In Equation (3), Ω_0 is the low-frequency plateau, which is proportional to the seismic
 247 moment M_0 , and f_c is the corner frequency. Additional information on how we corrected
 248 the spectra for geometrical spreading and attenuation to compute M_0 from Ω_0 is given
 249 in Section 1.6. The moment magnitude M_w is:

$$250 \quad M_w = \frac{2}{3} (\log M_0 - 9.1). \quad (4)$$

251 Once moment magnitude estimates M_{ref} were available for at least one event in a
 252 template family, we estimated a local magnitude $M_{L,i}$ for all other events i based on log
 253 amplitude ratios:

$$254 \quad M_{L,i} = M_{\text{ref}} + \text{Median}_{s,c} \left\{ \log \frac{A_{s,c}^i}{A_{s,c}^{\text{ref}}} \right\}, \quad (5)$$

255 or more generally if there are several reference events:

$$256 \quad M_{L,i} = \text{Median}_k \left\{ M_{\text{ref},k} + \text{Median}_{s,c} \left\{ \log \frac{A_{s,c}^i}{A_{s,c}^{\text{ref},k}} \right\} \right\}. \quad (6)$$

257 Using Equation (6) to compute a local magnitude M_L for every event with a moment
 258 magnitude M_w , we measured the scaling between M_w and M_L and built the calibration
 259 first-order relationship $M_w = A + BM_L$ (see Figure S1B).

260

2.3 Identifying Mining-Related Seismicity

261

262

263

264

265

Template matching lends itself particularly well to identifying sources of mining-related earthquakes. We identified these by analyzing the distribution of detection times within the day. Templates that detected more than 80% of events between 6am and 6pm were categorized as mining-related templates (see Figure S2 in Supplementary), since we do not expect natural seismicity to occur within preferred times.

266

2.4 Gutenberg-Richter b-value

267

268

The frequency-magnitude distribution of earthquakes typically follows the Gutenberg-Richter law (Gutenberg & Richter, 1941):

269

$$\log N(M) = a - bM. \quad (7)$$

270

271

272

273

In Equation (7), $N(M)$ is the number of earthquakes exceeding magnitude M , the a-value depends on the total number of observed events, and the b-value controls how frequent larger earthquakes are (typically $b \approx 1$). We estimated the b-value with the maximum likelihood technique (Aki, 1965):

274

$$b = \frac{1}{\ln(10) (\bar{M} - M_c)}. \quad (8)$$

275

276

277

278

279

280

281

282

283

Equation (8) is derived for continuous magnitudes M (no bias from binned magnitudes). M_c is the magnitude of completeness, *i.e.* the magnitude above which all events are detected. We computed M_c with the maximum curvature technique (*e.g.* Wiemer & Katsumata, 1999), that is, taking the mode of the (non-cumulative) frequency-magnitude distribution as the magnitude of completeness. We used the kernel density method to estimate the probability density function (pdf) of the frequency-magnitude distribution. We computed M_c on the pdf instead of the raw histogram to mitigate the bin-size dependence of the M_c estimate. The estimation of b-value and magnitude of completeness is illustrated on two earthquake populations in Figure 3.

284

285

286

287

288

289

290

At each template location, we selected all the templates within a 5 km-radius and used the events they detected to compute b and M_c . Following Tormann et al. (2013), we imposed a minimum of 50 events to compute the b-value and, in addition, requested a minimum of 30 events above the magnitude of completeness. As these numbers are still low, we carefully estimated the uncertainties to assess the statistical significance of b-value differences between different groups following Utsu (1966). The confidence interval for a single b-value can be derived from its probability density function ρ :

291

$$\rho(\hat{b}) = \frac{n^n}{\Gamma(n)} \left(\frac{b}{\hat{b}}\right)^{n+1} e^{-n\frac{b}{\hat{b}}}, \quad (9)$$

292

293

294

295

296

297

298

where \hat{b} is the b-value random variable, b is the estimate as given by Equation (8), n is the number of earthquakes with magnitude $M > M_c$, and Γ is the gamma function. Confidence intervals were derived from the percentiles of the cumulative distribution function (see Figure 3C).

Utsu (1966) also noted that the b-value ratio between two populations 1 and 2 follows the F distribution with degrees of freedom $2n_1$ and $2n_2$, where n_1 and n_2 are the numbers of earthquakes with $M > M_c$ in groups 1 and 2, respectively:

299

$$\frac{\hat{b}_2 b_1}{\hat{b}_1 b_2} \sim F(2n_1, 2n_2). \quad (10)$$

In Equation (10), the groups are indexed such that $b_1 > b_2$. The confidence level at which the two b-values are different is equal to the probability that $\hat{b}_1 > \hat{b}_2$:

$$\mathbb{P}(\hat{b}_1 > \hat{b}_2) = \mathbb{P}\left(\frac{\hat{b}_2 b_1}{\hat{b}_1 b_2} < \frac{b_1}{b_2}\right) \equiv \text{cdf}_{F(2n_1, 2n_2)}\left(\frac{b_1}{b_2}\right). \quad (11)$$

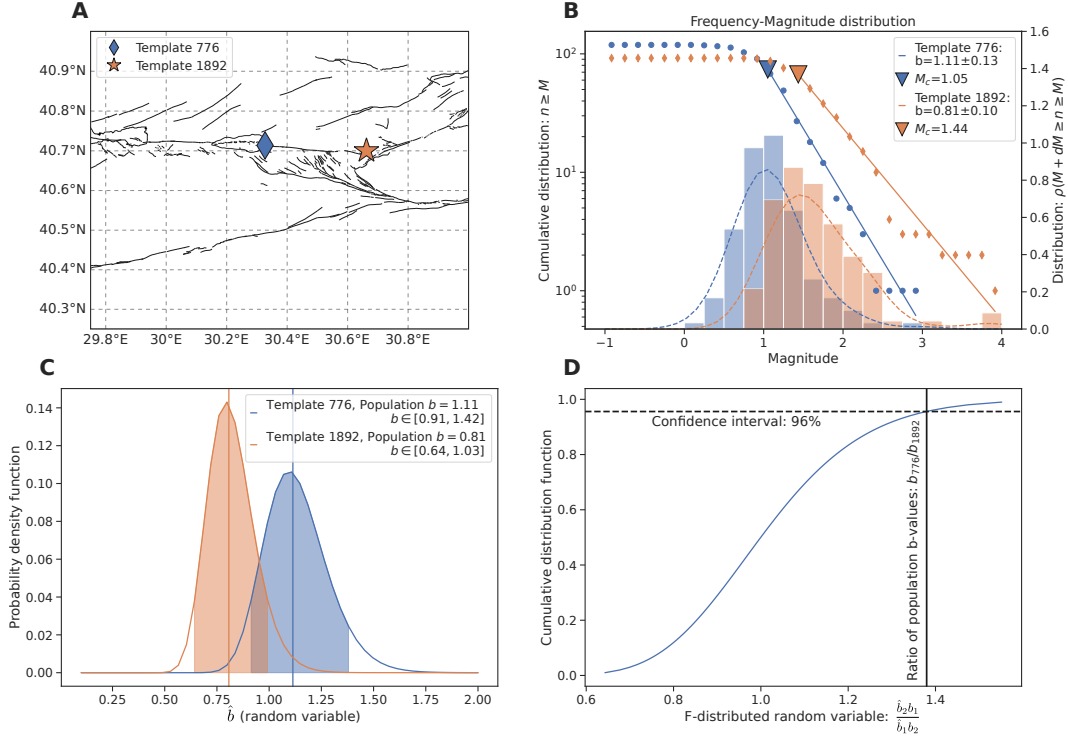


Figure 3. Estimation of the b -value and its uncertainties on two earthquake populations (two template families). **A:** Location of the two population centroids. Template 776 is located at the eastern side of Lake Sapanca and template 1892 is located near Akyazi. **B:** Cumulative (scatter plot) and non-cumulative (histogram) frequency-magnitude distributions. The dashed curves are the kernel density estimate of the non-cumulative probability density functions (pdf). The mode of the pdf is used as the magnitude of completeness (maximum curvature method). The b -value is computed with the maximum likelihood estimate (MLE, Equation (8)). **C:** The b -value pdf computed with Equation (9). The shaded area is the 90% confidence interval, also given in the legend. The b -value population is taken as the MLE (also shown with the vertical bars). **D:** Significance of the b -value difference between two populations using Equation (11). In this example, the b -value of template 776's event family is greater than template 1892's at the 96% confidence level.

300 In Equation (11), the right-hand term is the cumulative distribution function (cdf) of
 301 the F distribution. This method is exemplified at Figure 3D.

302 2.5 Temporal Clustering

303 In this manuscript, we refer to temporal clustering as the property of earthquake
 304 sequences in which events influence the timings (advance or delay) of future earthquakes,
 305 that is, the non-randomness of earthquake sequences (*e.g.* Gardner & Knopoff, 1974; Marsan
 306 & Lengline, 2008). We quantified the strength of temporal clustering in earthquake se-
 307 quences by analyzing the statistical properties of the number of earthquakes per unit time,
 308 which we refer to as the earthquake occurrence time series. It is given by:

$$309 e(t) = \text{Number of events in } [t; t + \Delta t], \quad (12)$$

where Δt is a user-defined time bin duration, and t is the calendar time. An example is given in Figure 4A. Burst-like sequences covering wide intervals of recurrence times are not random (see Figure 4B,C) but clustered in time. Time clustered seismicity exhibits time scale invariant characteristics. The spectrum of the earthquake occurrence $e(t)$ (as computed by Equation (12)) follows a power law of frequency ($\propto f^{-\beta}$, see Figure 4D), and the time series $e(t)$ shows a fractal statistics (Figure 4E). We measured the fractal dimension of the earthquake occurrence time series by subsequently dividing the time axis into smaller and smaller time bins (varying size τ), and counting the fraction of bins x that were occupied by at least one earthquake (Smalley Jr et al., 1987; Lowen & Teich, 2005). For a certain range of time bin sizes τ , we observe:

$$x \propto \tau^{1-D}. \quad (13)$$

In Equation (13), D is the fractal dimension of the time series. The fractal dimension varies between the two end-members $D = 0$ for a point process (*e.g.* Poisson point process for the background seismicity), and $D = 1$ for a line (uninterrupted seismicity). A large fractal dimension ($D > 0.2$) characterizes cascade-like activity where past events strongly influence the timings of future events. Fractal analysis has been used in multiple studies to characterize earthquake clustering (Smalley Jr et al., 1987; Lee & Schwarcz, 1995; Beaucé et al., 2019). Note that periodic seismicity does not follow a fractal behavior and cannot be characterized by this method. Building the $x(\tau)$ curve (Equation (13), Figure 4E) is computationally more simple than estimating the spectrum (Figure 4D). Likewise, it is simpler to fit $x(\tau)$. Therefore, we chose to compute the fractal dimension D to characterize temporal clustering in the rest of this study.

The method described in Section 2.5 does not explicitly deal with space. However, we applied this analysis to subsets of the earthquake catalog containing neighboring earthquakes (as described for the b-value, see Section 2.4), and thus obtained a fractal dimension for each template.

3 Results

3.1 The Earthquake Catalog

3.1.1 Regional Seismicity

Following the method described in Section 2.2, we built a database of 3,546 templates and with them detected 35,437 events, including both natural and anthropogenic seismicity. We applied our analysis between 38.50°N-41.50°N and 28.00°E-32.00°E (see Figure 1A). Figure 5 shows the locations of the 3,320 template earthquakes that are shallower than 20 km and have horizontal uncertainties less than 15 km, as well as the cumulative detection count per template over the whole study period. We purposely present an earthquake catalog for this region that extends far beyond the NAFZ to provide a comprehensive description of the earthquake signals found in the data set. We found that most of the 1,972 events detected with templates located deeper than 20 km originated far outside the study region, in particular in the Hellenic and Cyprus subduction zones in the southwest and south of the study region, respectively. Therefore, we discarded these deeper templates for any further analysis. Furthermore, we found that about half of the detected seismicity was due to mining activity (see Section 2.3): among the 31,329 earthquakes detected with the 3,320 templates, we identified 16,674 natural earthquakes and 14,655 mining-related earthquakes. The locations of mining activity that we identified (see Figure 5) agree well with the analysis of Poyraz et al. (2015) (their Figure 3) whereas the Kandilli catalog (see Data and Resources) tends to report less explosions, in particular beneath the DANA array (see Figure S3).

The majority of earthquakes occurred outside the station array and not in the NAFZ itself, that is, north of 40.80°N or south of 40.30°N (see Figure 5B). Location uncertainties increase with increasing distance from the DANA array: inside 40.30°N-41.00°N and 30.00°E-30.50°E, the average horizontal uncertainty is $\bar{h}_{\max} = 0.97$ km and the average

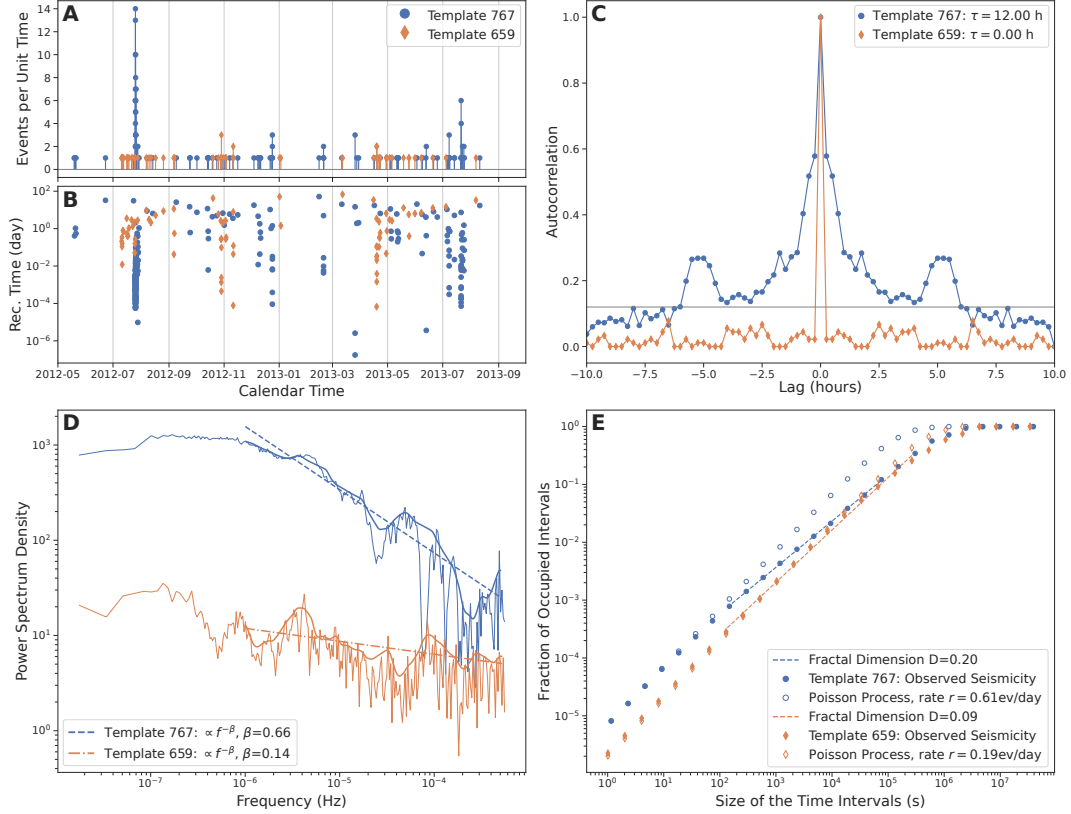


Figure 4. Quantifying the strength of temporal clustering in a strongly clustered sequence (Template 767, blue dots) and a weakly clustered sequence (Template 659, orange diamonds). **A:** Number of earthquakes per unit time (referred to as earthquake occurrence, see Equation (12)). **B:** Recurrence times vs. origin times. **C:** Autocorrelation of the earthquake occurrence time series. The horizontal black line is the arbitrary threshold used to define the correlation time τ . **D:** Power spectral density of the earthquake occurrence. The linear trend, in the log-log space, is the exponent of the power-law that indicates a scale invariant process. **E:** Fractal analysis of the earthquake occurrence (see text and Equation (13)). We measure the slope between $dt_{\min}=100$ s and $dt_{\max} = 1/r$, where $r = N/T$ is the average seismic rate (number of events N divided by time span T). For reference, for each template we simulate the seismicity from a Poisson point process with average rate r . The slope of the Poisson point process gives a fractal dimension $D = 0$ (*i.e.* dimension of a point).

361 vertical uncertainty is $\bar{v}_{\max} = 0.74$ km, whereas these uncertainties increase to $\bar{h}_{\max} =$
 362 8.53 km and $\bar{v}_{\max} = 4.57$ km outside this box (see Figure 5C,D).

363 Since accurate moment magnitude estimation rely on correct source-receiver dis-
 364 tances (see Section 2.2.5), we only computed moment magnitudes for events with $h_{\max} <$
 365 5 km (see Figure 5D). After the SNR criterion, we could estimate moment magnitudes
 366 within 168 template families of natural seismicity, from which we computed 1,929 local
 367 magnitudes. These magnitudes range from -1 to 4 , and we obtained $b = 0.85$ and $M_c =$
 368 1.18 (see Section 2.4 and Figure S4). We computed a M_w - M_L calibration close to iden-
 369 tity, $M_w = 0.15 + 0.93M_L$ (see Section 2.2.5 and Figure S1B). The magnitude of com-
 370 pleteness of our catalog indicates that we were not able to estimate magnitudes below
 371 $M \approx 1$ but still detected them: only 12% of the detected seismicity has a magnitude
 372 estimate. Therefore, $M_c = 1.18$ is only an upper bound to the magnitude of complete-

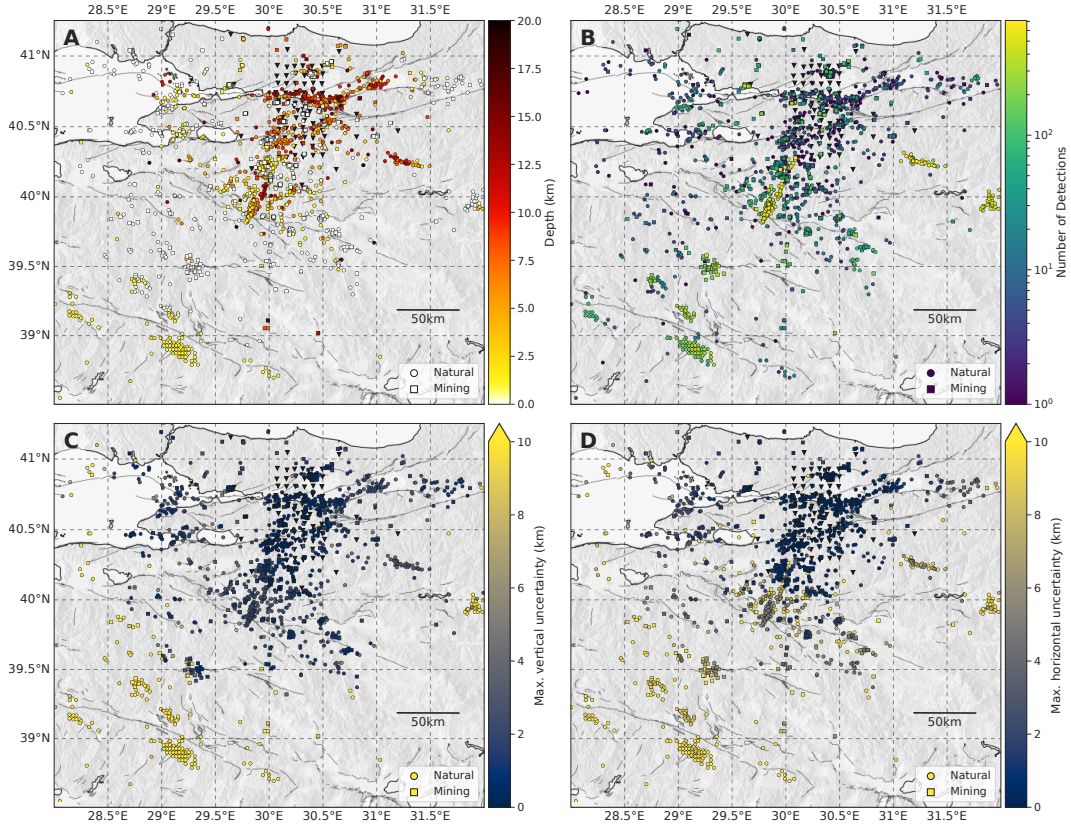


Figure 5. Map view of the locations of the template earthquakes detected and used in this study. Only templates with maximum horizontal uncertainty less than 15 km and depth less than 20 km are shown (total of 3,320 templates). Filled dots are for natural earthquakes (1,471 templates), and squares are for mining-related events (1,849 templates; see text for details about identifying templates as mining templates). **A:** Event depths. **B:** Cumulative number of event detections per template. Most of the detected earthquakes actually originate from outside the North Anatolian Fault Zone. **C:** Maximum vertical uncertainty v_{\max} , i.e. depth range spanned by the projection of the uncertainty ellipse onto a vertical plane. **D:** Maximum horizontal uncertainty h_{\max} , i.e. length of the major semi-axis of the projection of the uncertainty ellipse onto the horizontal plane.

373 ness of the whole catalog. For reference, we estimated a b-value and magnitude of completeness of $b = 0.91$ and $M_c = 1.05$ with the catalog published in Poyraz et al. (2015),
 374 with magnitudes ranging from 0 to 4 (see Figure S4). Our magnitudes seemed to be systematically larger than theirs for smaller events, with an average difference of 0.5 unit
 375 over all compared events (see Figure S4C). Detailed b-values and magnitudes of completeness are presented in Section 3.2.

376
 377
 378
 379 We present the spatio-temporal distribution of the seismicity in Figure 6. An overall decaying activity of natural earthquakes is superimposed to a uniform mining-related
 380 activity (compare Figure 6A vs. B). We observe two sequences of slowly decaying activity below 39°N and around 40°N. The southernmost earthquake sequence (39°N) is
 381 part of the aftershock activity of the M5.1 2012-05-03 39.18°N/29.10°E/5.4 km earthquake (just before the deployment of DANA). The 40°N sequence is not featured in the Kandilli
 382 nor in the United States Geological Survey catalog.
 383
 384
 385

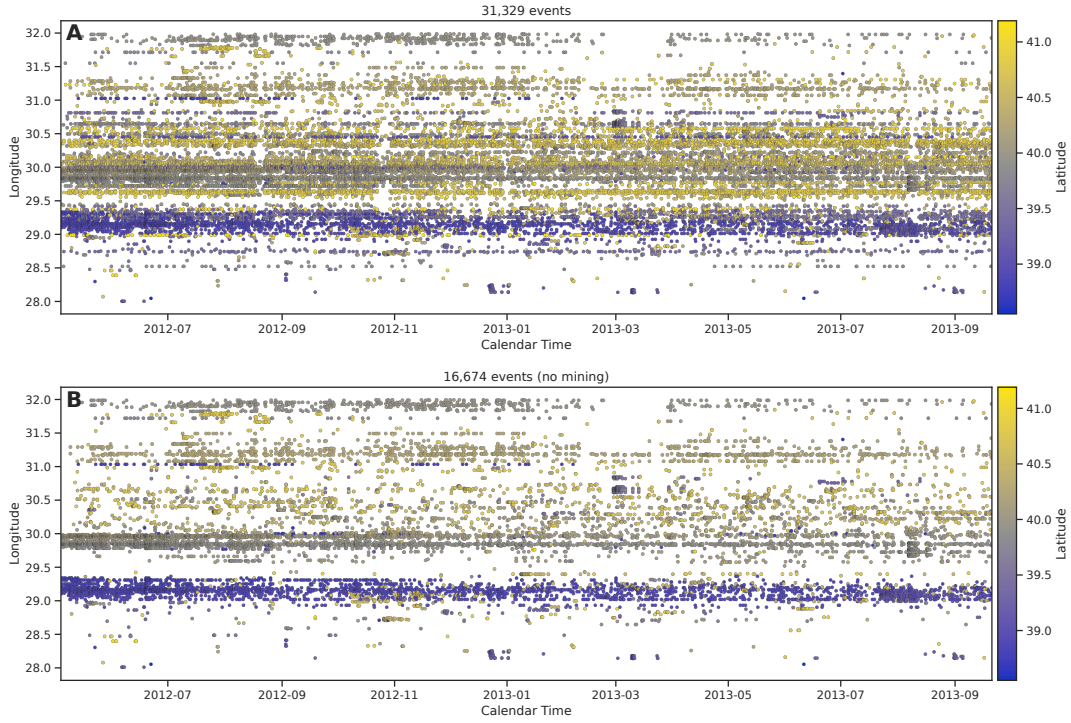


Figure 6. Spatio-temporal distribution of the earthquake activity in the study region. The longitude of each event is shown against its origin time, and the color codes the latitude. **A:** We detected 31,329 events with the 3,320 template earthquakes presented in Figure 5 from 2012-05-04 to 2013-09-20. **B:** The templates due to natural seismicity detected 16,674 earthquakes. The seismic activity taking place on the NAFZ (latitudes 40.35°N-40.80°N) represents a small amount of the total seismicity ($\sim 2,000$ events).

386 Our earthquake catalog and detection and location codes are available online (see
 387 Data and Resources, and see Supplementary Material for additional information about
 388 the structure of the catalog file). This analysis of the regional seismicity shows that most
 389 of the detected seismic activity occurred outside the North Anatolian Fault Zone, which
 390 may be a feature of this section of the NAFZ being early in its earthquake cycle (Ben-
 391 Zion & Zaliapin, 2020). In the following, we focus on the template earthquakes located
 392 in the vicinity of the NAFZ and near the station array (40.25°N-41.00°, 29.80°E-31.00°E).

393 *3.1.2 Seismicity of the North Anatolian Fault Zone*

394 Figure 7 shows the locations of the template earthquakes in the fault zone, as well
 395 as the 2,141 earthquakes relocated with the double-difference method (see Section 2.2).
 396 The median horizontal and vertical errors on relative locations are 73 m and 91 m, res-
 397 pectively, meaning that they can reliably be interpreted in terms of active structures.
 398 Earthquake hypocenters reveal a complex network of faults, with much of the seismic-
 399 ity occurring on secondary faults rather than on the NAFZ itself. We divided the fault
 400 zone into nine subregions (*cf.* Figure 7A) whose names we will keep referring to in this
 401 manuscript. These are organized into four along-strike sections: Izmit-Sapanca, fault-
 402 parallel Sapanca-Akyazi, Karadere, and the entire southern strand, and six fault-perpendicular
 403 sections: Lake Sapanca west and east, fault perpendicular Sapanca-Akyazi, Akyazi, and
 404 the southern strand west and east. The northern strand is overall more active than the
 405 southern strand, and the Sapanca-Akyazi segment hosts the densest activity. In partic-

ular, both terminations of the segment, the eastern side of Lake Sapanca and the area around the Akyazi fault, host strong seismicity. The Akyazi region features the deepest seismicity in the vicinity of the NAFZ (down to 20 km). The group of earthquakes located at the northernmost of the Sapanca-Akyazi region (Figure 7A-B) are part of the 2012-07-07 M_L 4.1 Serdivan earthquake sequence. Most of the seismicity along the southern strand occurs in areas where surface fault traces indicate more structural complexity. Note that the relocated seismicity tends to be distributed in patches, which is partly due to the detection method. Indeed, template matching tends to detect groups of collocated earthquakes, whereas small events located in between template earthquakes may remain undetected.

The fault parallel and fault perpendicular cross-sections in Figure 7C show the events' depth distribution. The seismicity is enhanced in the lower half of the seismogenic zone: 7-15 km along the northern strand, and even deeper than 15 km around the Akyazi fault, and 5-10 km depth along the southern strand. The main exception to that depth distribution are the earthquakes at the western side of Lake Sapanca, with hypocenters clustered around 5 km depth. The Lake Sapanca W. fault perpendicular cross-section (see Figure 7C) shows that this shallow seismicity seems restricted to the southern side of the fault, namely the Armutlu Bloc.

The map views and cross-sections in Figure 7 suggest a narrower deformation zone in the north where seismicity is mostly distributed within 5-10 km of the main fault trace, whereas we observe a wider deformation zone along the southern strand with seismicity distributed within 15-20 km of the fault trace. We emphasize that the detected microseismicity illuminates the deformation zone associated with the NAFZ rather than the fault itself. The Sapanca-Akyazi and Akyazi fault perpendicular cross-sections could indicate a north dipping deformation zone, although these mostly show almost horizontally aligned earthquakes. Under the assumption that the deformation zone does dip towards the north, we approximately measure a 60° dip angle in the middle of the Sapanca-Akyazi segment, and 85° near the Akyazi fault. Identifying a global dip direction of the deformation zone along the southern strand is equally ambiguous. In the east, one could either identify slightly south dipping structures ($\sim 85^\circ$) or more strongly north dipping structures ($\sim 70^\circ$).

We present the temporal distribution of the seismicity in Figure 8. The recurrence times are given against their detection times for each of the nine cross-sections introduced above. The recurrence time is the time interval between two consecutive co-located earthquakes. In practice, recurrence times are computed as the time intervals between consecutive events detected by a same template. The most striking feature of Figure 8 is the organization of some earthquake sequences into bursts of seismicity with recurrence times spanning many orders of magnitude. These sequences are time clustered (*e.g.* W. B. Frank et al., 2016; Beaucé et al., 2019) and recurrence times are power-law distributed (*e.g.* Utsu et al., 1995). These bursts are usually associated with sequences of foreshocks-mainshock-aftershocks, although in general earthquake sequences can have no clear mainshock (that is, an event of magnitude larger than all other events of the sequence) and still exhibit a strong burst-like behavior. The seismicity at the eastern end of Lake Sapanca and near Akyazi is almost exclusively organized into such sequences of burst-like seismicity, whereas the southern strand hosts much less of these burst-like episodes. Figure 8 also reports the local magnitudes (see Section 2.2.5). The Sapanca-Akyazi segment and its vicinity is the most active region with the largest magnitude events observed during the study period. Among the nine $M_L \gtrsim 3$ natural earthquakes we detected, three occurred near each other, close to the city of Serdivan, including the largest event of the study: the 2012-07-07 M_L 4.1 Serdivan earthquake ($30.404^\circ\text{E}/40.763^\circ\text{N}/11.3\text{ km}$). The area around the Akyazi fault also produced four $M_L > 3$ earthquakes, whereas earthquakes near Lake Sapanca did not exceed $M_L = 3$.

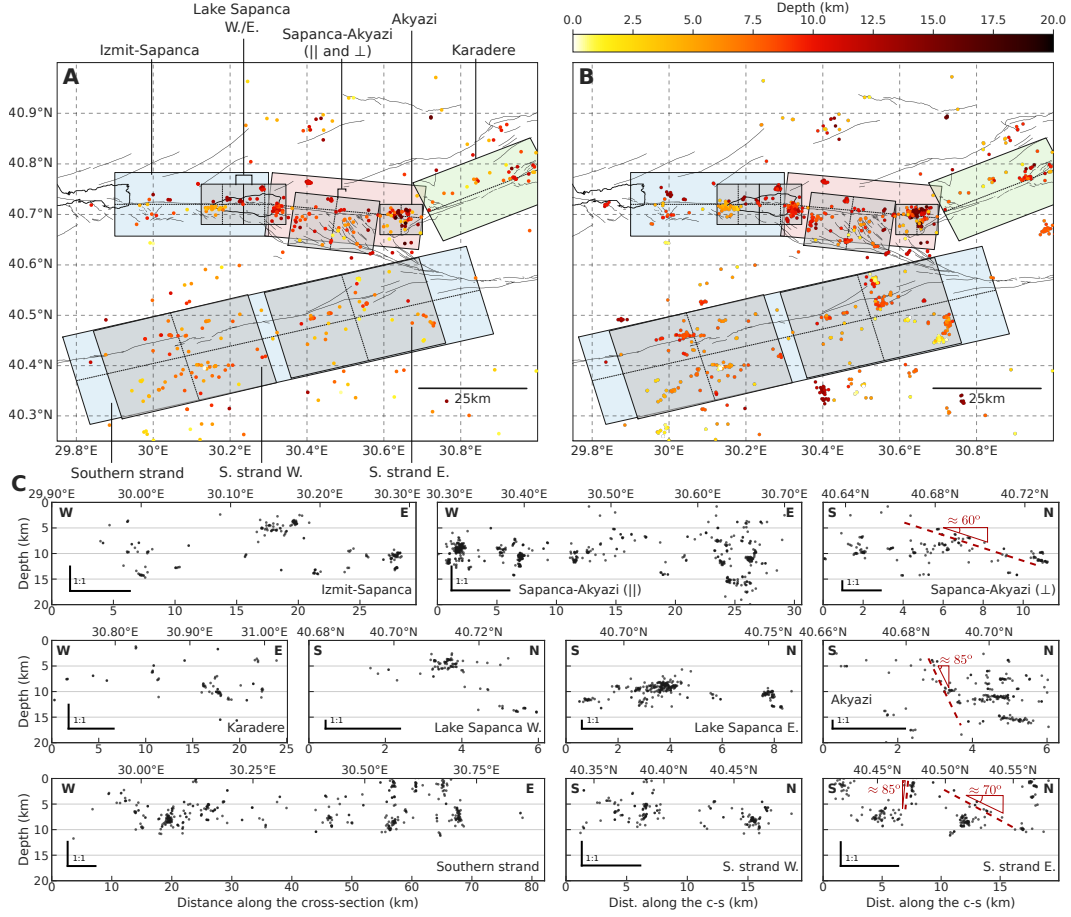


Figure 7. Earthquakes in the North Anatolian Fault Zone. **A:** Locations of the template earthquakes with color coded depths. We define nine subregions along the different segments of the fault. Only in this figure the Sapanca-Akyazi region is subdivided into a fault parallel and a fault perpendicular sections. The thin black dotted lines inside each colored box define either fault parallel or fault perpendicular cross-sections (see bottom panels, C). The color shading of each box is only to help distinguish between them. **B:** Earthquake hypocenters successfully relocated with the double-difference method and color coded by depth. Events for which relocation was not successful were attributed the template location. **C:** Depth cross-sections of the different areas introduced above. The earthquake locations contained in the boxes are projected onto the boxes' central axis. The bottom x-axes are distances along the cross-section axes in kilometers, and the top x-axes are the geographic coordinates relevant to each cross-section (either longitude or latitude). Note that the x scales and the aspect ratio across cross-sections vary. The 1:1 aspect ratio is drawn in the lower left corner of each cross-section. The dashed red lines and angles are given for reference but are not our take-away message.

458

3.1.3 Comparison with Past Seismicity

459

460

461

462

463

We combined different earthquake catalogs to compare the 2012-2013 detected seismicity with the pre-Izmit, Izmit-Düzce, and early post-Düzce seismicity (Bulut et al., 2007; Ickrath et al., 2015; Bohnhoff et al., 2016, and see Figure 9). We note that the Izmit-Düzce earthquake catalog is more complete in the west (around the Izmit-Sapanca segment) than the pre-Izmit and early post-Düzce catalogs due to the higher number of sta-

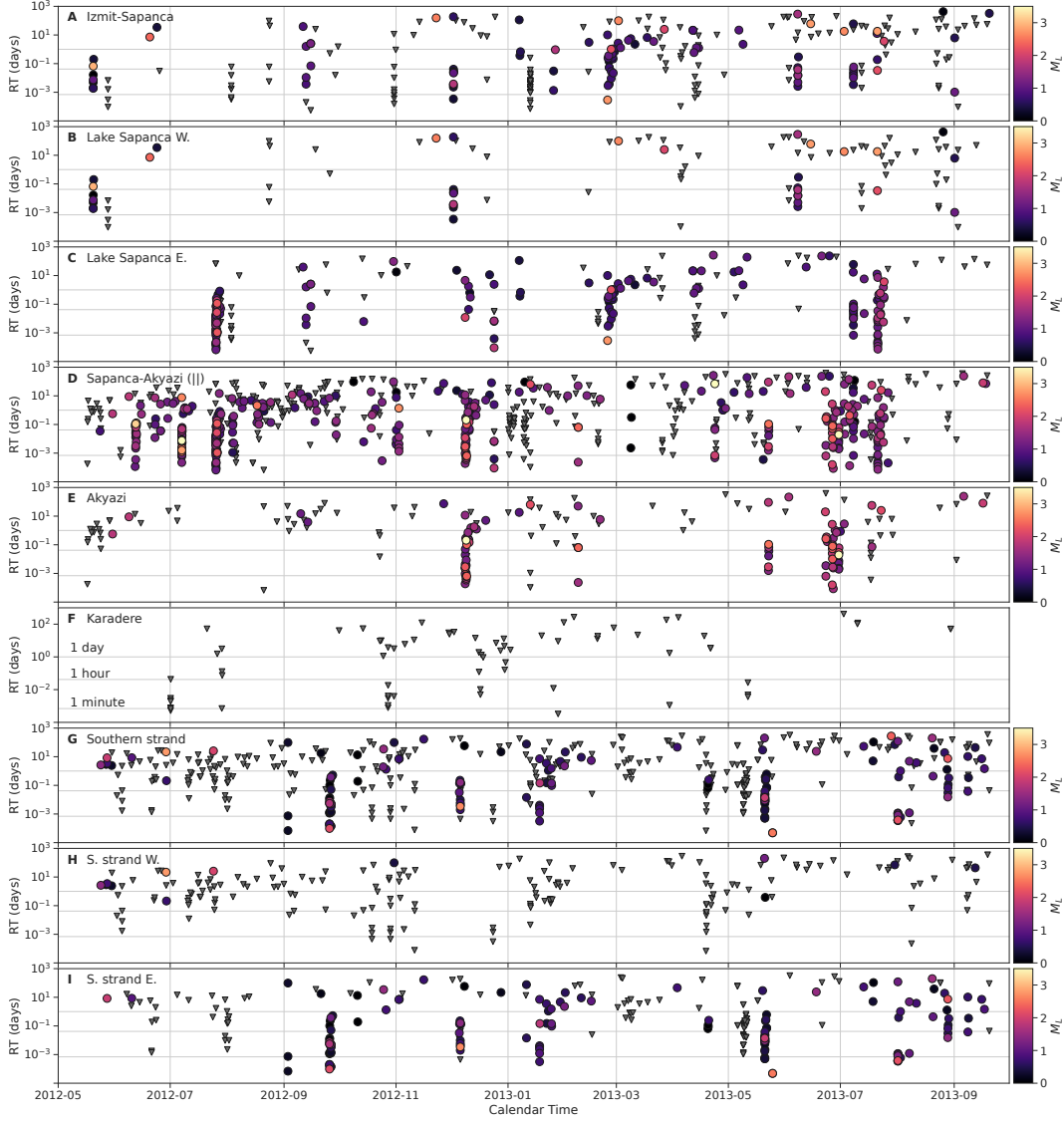


Figure 8. Time evolution of the earthquake recurrence times for different subsets of the earthquake catalog (refer to Figure 7 for the name of the areas). The recurrence time is the time between two consecutive events detected by a same template. Note that the y-axis is in log scale and that some seismic episodes span many orders of magnitude of recurrence time. These episodes are characteristic of burst-like, or cascade activity (see text). The color scale indicates the local magnitude, and inverted grey triangles are events for which no reliable estimates were obtained.

464 tions used in this time period (see, *e.g.* Ickrath et al., 2015, and Figure 9B). It is also
 465 worth mentioning that these three catalogs show both natural and mining-related seis-
 466 micity whereas we have discarded the man-made seismicity to the best of our ability (see
 467 Section 2.3). During these three time periods, the (moment) magnitudes of complete-
 468 ness of these catalogs are $M_c = 1.56, 1.69,$ and $1.44,$ respectively, and few $M_w < 1$ earth-
 469 quakes are reported (see Figure S5). Using our M_w - M_L calibration to convert our local
 470 magnitudes to effective moment magnitudes, we obtained $M_c = 1.18$ and 27% of
 471 the earthquakes contributing to the frequency-magnitude distribution have $M_w < 1$ (see

472 Figure S5D). Therefore, also recalling that most of the detected events are too small to
 473 be characterized by their magnitude, our catalog reports smaller events than the cata-
 474 logs we compare it with.

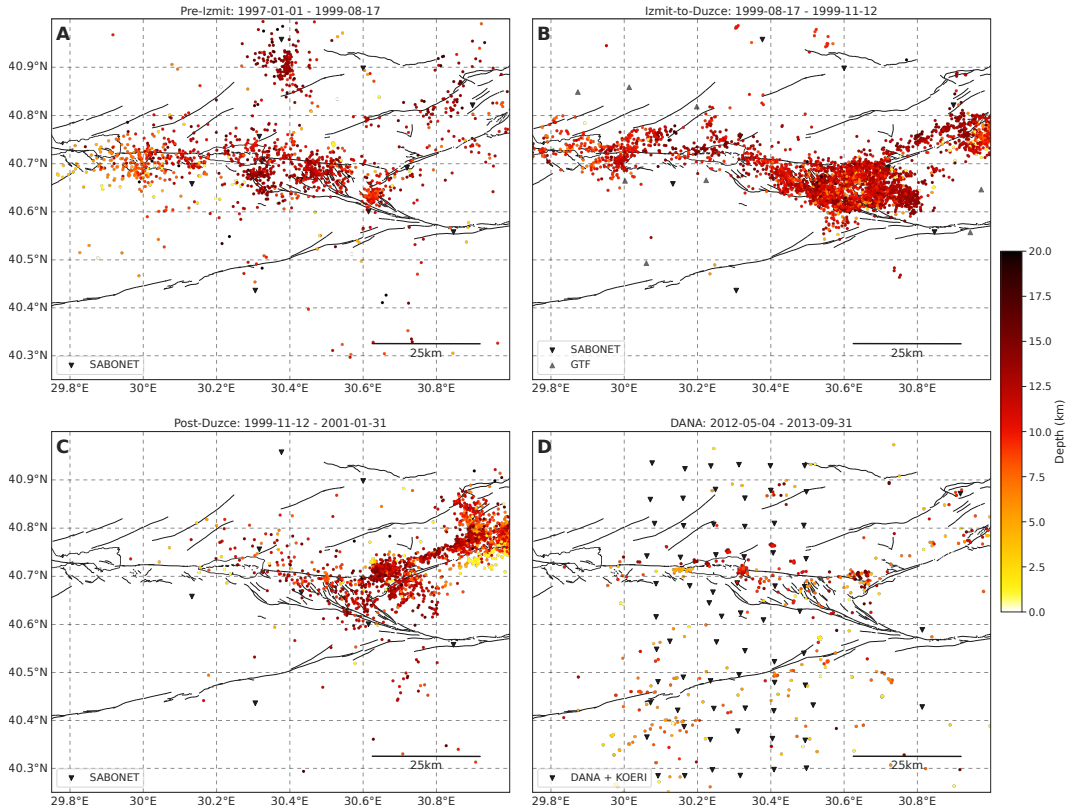


Figure 9. Comparison of the **A:** pre-Izmit, **B:** Izmit-Düzce, the SABONET stations were complemented by 21 temporary stations from the German Task Force (GTF, grey triangles), **C:** early post-Düzce, and **D:** late post-Düzce seismicity. The inverted black triangle are the seismic stations and the colored dots are the earthquake locations.

475 The middle sections of the Izmit-Sapanca and Sapanca-Akyazi segments were particu-
 476 larly active seismically before the Izmit earthquake, and some clusters of earthquakes
 477 were observed beneath Lake Sapanca (Figure 9A). The Izmit earthquake is known to have
 478 nucleated near a swarm of seismicity that was active before the M7.4 event (Crampin
 479 et al., 1985; Lovell et al., 1987; Ito et al., 2002). In the three months between the Izmit
 480 earthquake and the Düzce event, the seismic activity was strongest in the area around
 481 the triple junction between the Sapanca-Akyazi segment, the Karadere segment, and the
 482 Mudurnu fault (Figure 9B). The Izmit hypocentral region remained active and, compar-
 483 atively, little activity was detected near Lake Sapanca. After the Düzce earthquake, most
 484 activity along the Izmit-Sapanca and Sapanca-Akyazi terminated, and seismicity con-
 485 centrated along the Karadere segment (Figure 9C). The Akyazi region, where little co-
 486 seismic slip was observed (Ozalaybey et al., 2002; Bohnhoff et al., 2006, 2008), hosted
 487 a cluster of strong activity, possibly driven by the Izmit residual stresses. Note that no
 488 seismicity was detected near Lake Sapanca. About 13 years after the Izmit and Düzce
 489 earthquakes, we detected the strongest activity at the eastern side of Lake Sapanca, and
 490 near the Akyazi fault (Figure 9D). If not due to the absence of $M < 1$ earthquakes in
 491 these catalogs, the lack of intense seismicity near Lake Sapanca in the early post-Düzce
 492 period suggests that faults near Lake Sapanca did not slip during the afterslip-driven af-
 493 tershock sequence with Omori-like decaying seismicity (Perfettini & Avouac, 2004). More-

494 over, the Omori law predicts a seismicity rate about four orders of magnitude lower 13
 495 years after the mainshock (using Omori law parameters from Bayrak & Öztürk, 2004),
 496 therefore the seismic activity near Lake Sapanca should have been high after the Izmit
 497 earthquake if the 2012-2013 seismicity were to be remnants of aftershocks. The 2012-
 498 2013 Lake Sapanca seismicity also appears much stronger than the pre-Izmit seismicity
 499 (Figure 9A).

500 3.2 Observed b-values

501 Computed b-values and magnitudes of completeness (see Section 2.4) are presented
 502 in Figure 10. Of most interest to this study, we see that earthquakes at the eastern side
 503 of Lake Sapanca exhibit high b-values ($b \approx 1.1$), whereas earthquakes near the Akyazi
 504 fault show low b-values ($b \approx 0.8$). The magnitude of completeness varies from $M_c \approx$
 505 1.3 near Akyazi to $M_c \approx 1.0$ near Lake Sapanca. We note that visual checking of the
 506 frequency-magnitude distributions showed that, in general, they follow the Gutenberg-
 507 Richter law well, except for the Serdivan earthquakes where a peak around $M_L \approx 2.5$
 508 can be observed. The significance of the b-value difference between the eastern Lake Sapanca
 509 and Akyazi was assessed by applying the statistical test presented in Section 2.4 (see Equa-
 510 tion (11)). We found that the difference was significant at the 96% confidence level (see
 511 Figure 3D).

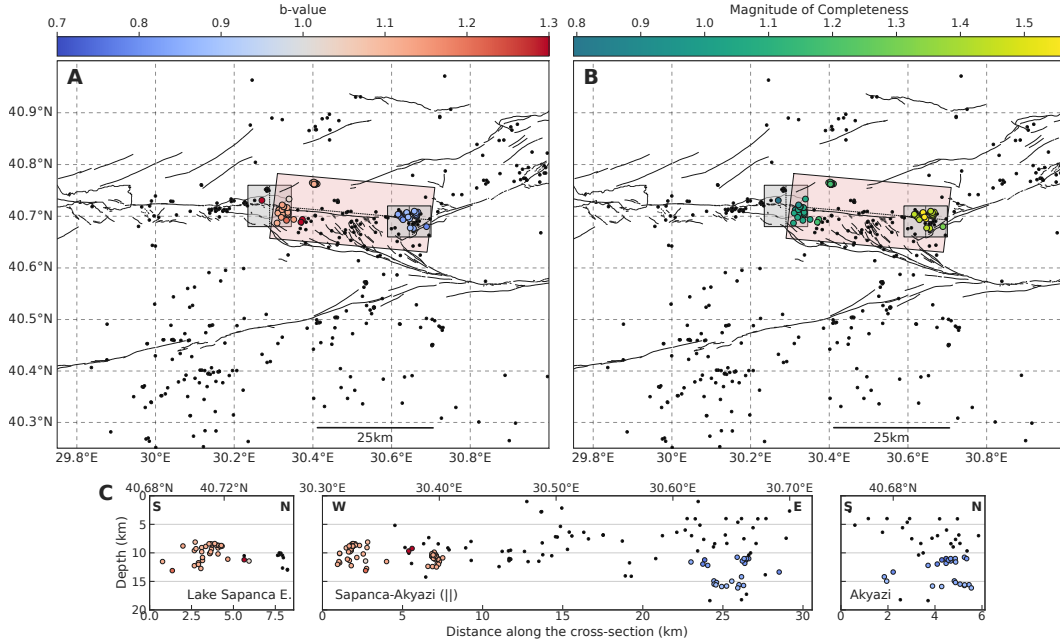


Figure 10. **A:** Map view of template earthquakes with color coded Gutenberg-Richter b-value. Smaller black dots are event families for which we could not compute moment magnitudes (see text). **B:** Map view of template earthquakes with color coded magnitude of completeness. In both top panels, the shaded areas refer to the regions introduced in Figure 7. **C:** Template earthquakes with color coded b-value on fault parallel and fault perpendicular cross-sections. Hypocenters are projected along the dotted axes shown on the map view.

512 3.3 Observed Temporal Clustering

513 We characterized temporal clustering as a function of space (see Figure 11) follow-
 514 ing the method described in Section 2.5. The strongest temporal clustering (fractal di-

515 mension $D > 0.20$) is observed on the eastern side of Lake Sapanca, beneath the so-
 516 called Rangefront trace. Other areas of strong activity, like the Serdivan earthquakes (around
 517 $30.404^{\circ}\text{E}/40.763^{\circ}\text{N}$) and the Akyazi area, only show small-to-moderate temporal clus-
 518 tering ($D < 0.14$), thus confirming the outstanding character of the eastern Lake Sapanca.
 519 We note that while the temporal organization of recurrence times shown in Figure 8 indicat-
 520 ed burst-like seismicity in all of the above mentioned areas, this quantitative analys-
 521 is was necessary to distinguish between strongly and moderately time clustered sequences.
 522 A few other isolated locations exhibit strong temporal clustering, and seem to be sys-
 523 tematically occurring near the bottom of the seismogenic zone (*cf.* Figure 11C). Compar-
 524 ing the cumulative number of detections per template and their fractal dimension shows
 525 that there is no trivial correlation between the two (see Figure 11A vs. B). We note that
 526 we did the same fractal analysis on all templates of the study region and found another
 527 region of strong temporal clustering on the NAFZ, in the eastern Marmara Sea, where the
 528 1999 Izmit earthquake arrested (see Figure S6).

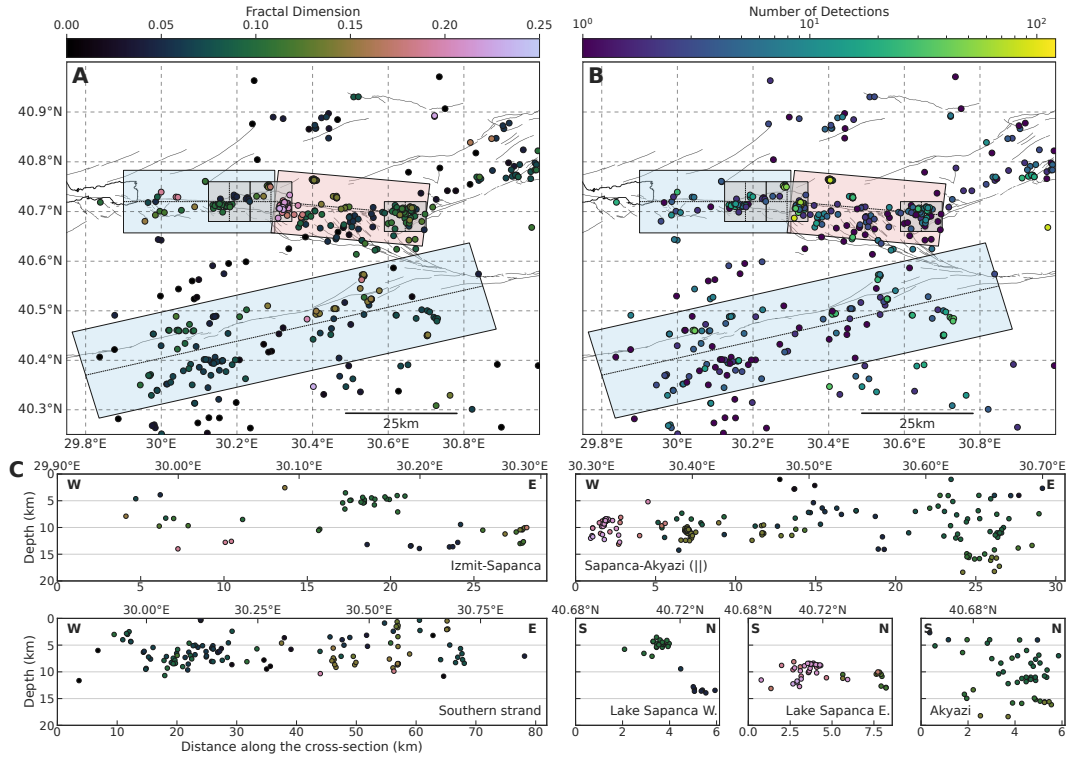


Figure 11. **A:** Map view of template earthquakes with color coded fractal dimension (*cf.* Equation (13)) showing the strength of temporal clustering. **B:** Map view of template earthquakes with color coded cumulative number of detections. In both top panels, the shaded areas refer to the regions introduced in Figure 7. **C:** Template earthquakes with color coded fractal dimension on fault parallel and fault perpendicular cross-sections. Hypocenters are projected along the dotted axes shown on the map view. High fractal dimensions mean strongly time clustered activity (*i.e.* past events strongly influence the timings of future events).

4 Interpretation and Discussion

529
 530 In the present section, we discuss implications of the observed spatial earthquake
 531 distribution for the mechanical state of the NAFZ (Section 4.1), we interpret the b-values

532 in terms of low and high stresses (Section 4.2), and we explain how temporal clustering
 533 can be related to fault rheology (Section 4.3).

534 4.1 Spatial Distribution of Seismicity

535 Apart from the Karadere segment, the seismicity is taking place off the main fault
 536 on a complex network of secondary faults, similarly to the Izmit-Düzce aftershocks (*e.g.*
 537 Ozalaybey et al., 2002; Bulut et al., 2007, and see Figure 7). This feature is in stark con-
 538 trast with the simplicity of the Izmit and Düzce earthquakes, which occurred on sim-
 539 ple fault segments (Barka et al., 2002; Langridge et al., 2002). Off-fault seismicity has
 540 also been observed to be a characteristic of fault zones early in their seismic cycle (Ben-
 541 Zion & Zaliapin, 2020) and might be due to off-fault, distributed deformation contribut-
 542 ing to accommodate slip deficits resulting from heterogeneous slip along the fault (Dolan
 543 & Haravitch, 2014).

544 Shallow creep has been observed along the Izmit-Sapanca and the Sapanca-Akyazi
 545 segments (*e.g.* Çakir et al., 2012; Hussain et al., 2016; Aslan et al., 2019). The creep rates
 546 and creep locations along the Izmit rupture have evolved with time (*e.g.* Bürgmann et
 547 al., 2002). Aslan et al. (2019) use 2011-2017 InSAR data and 2014-2016 GPS data and,
 548 thus, is the closest study to ours in time. The authors' model shows shallow creep down
 549 to 5 km along the Izmit-Sapanca segment and down to 2 km at the western end of the
 550 Sapanca-Akyazi segment. Such shallow creep should drive microseismicity in the vicini-
 551 ty of the creeping fault sections (*e.g.* Lohman & McGuire, 2007). The depth cross-sections
 552 (Figure 7C) only show shallow seismicity at the western Lake Sapanca (≈ 5 km depth).
 553 Although these depths are consistent with the creep depth given in Aslan et al. (2019),
 554 a direct causality link to the shallow creep is not straightforward because it is taking place
 555 off-fault (Figure 7B). Seismicity along the Sapanca-Akyazi segment do not support creep-
 556 driven activity at shallow depths (≈ 2 km). However, hypocenters suggest that, at the
 557 time of the study, the base of the seismogenic zone is around 10-15 km, which is in good
 558 agreement with Aslan et al. (2019).

559 Comparing our catalog with the seismicity in the past (see Section 3.1.3) showed
 560 that the eastern Lake Sapanca did not appear to be a particularly active area, either be-
 561 fore or right after the Izmit earthquake. However, this comparison relies on catalogs made
 562 with different methods and station coverage, and, consequently, different magnitudes of
 563 completeness. The seismic activity at the eastern Lake Sapanca may be a permanent fea-
 564 ture of the step-over that can only be observed with low magnitude of completeness cat-
 565 alogs ($M_c \lesssim 1.0$). We further discuss in Section 4.4 whether the seismicity at the east-
 566 ern Lake Sapanca is a new feature of the fault zone caused by the post-Izmit deforma-
 567 tion or is a constant phenomenon that could not be observed in such detail in the past.
 568 Variations in seismicity along the southern strand are harder to interpret because the
 569 lack of earthquakes in previous catalogs (see Figure 9) is partly due to the absence of
 570 stations in the past.

571 4.2 Gutenberg-Richter b-value

572 Laboratory experiments have shown that the b-value seems to be controlled by the
 573 state of stress, specifically that b decreases with increasing differential stress (*e.g.* C. H. Scholz,
 574 1968; Amitrano, 2003). Decreasing b-value with depth (Mori & Abercrombie, 1997; Wiemer
 575 & Wyss, 1997) and high b-value along creeping sections (*e.g.* Amelung & King, 1997;
 576 Wiemer & Wyss, 1997) also support the negative correlation of b with stress. Thus, the
 577 b-value can be used as a stressmeter.

578 Our results (Figure 10) show a clear difference in b-values between the eastern Lake
 579 Sapanca ($b \approx 1.1$) and the Akyazi ($b \approx 0.8$) seismicity. We recall that this difference
 580 is significant at the 96% confidence level (see Section 3.2). We interpret the higher b-
 581 values at Lake Sapanca as an indication of low background stresses, while we interpret
 582 the lower b-values at Akyazi as indicating high background stresses. Low stress at the

583 eastern Lake Sapanca suggests that aseismic slip might play a role in driving the seis-
 584 micity, implying that, there, faults have weak sections. High stress near Akyazi can be
 585 understood as resulting from the stress concentration that occurred during the Izmit earth-
 586 quake, when little co-seismic slip occurred along the Akyazi fault and the Akyazi gap.

587 4.3 Temporal Clustering, Earthquake Interactions, and Fault Mechan- 588 ical Properties

589 Strongly time clustered seismicity with a wide range of recurrence times, as pre-
 590 sented in Section 3.3, cannot be explained only by fluctuations of the background seis-
 591 micity rate, for example due to the injection of fluids at depth. Indeed, a Poisson point
 592 process with a transient increased rate only shifts the distribution of recurrence times
 593 towards shorter times but does not widen the distribution and does not have a large frac-
 594 tal dimension (see Figure S7). Temporal clustering, that is, cascading of events, emerges
 595 when different faults or sections of a fault interact (*e.g.* Burridge & Knopoff, 1967; Marsan
 596 & Lengline, 2008; Fischer & Hainzl, 2021). Earthquakes can trigger each other due to
 597 the static stress changes induced by the co- and postseismic displacements (*e.g.* King
 598 & Cocco, 2001), but also due to the dynamic stress changes induced by the elastic waves
 599 radiated by the rapid coseismic motions (*e.g.* Fan & Shearer, 2016). Furthermore, be-
 600 cause of the stress redistribution following any slip motion (not necessarily at seismic speeds),
 601 interaction can occur between a seismogenic asperity and its creeping surroundings: ac-
 602 celerated creep (*e.g.* afterslip) increases the stressing rate on the asperity (*e.g.* Catta-
 603 nia, 2019; Cattania & Segall, 2021). In realistic, complex conditions where seismic and
 604 aseismic slip co-occurs on short length scales (*e.g.* Collettini et al., 2011), numerical mod-
 605 els show that both co-seismic and creep mediated stress changes are important factors
 606 controlling the clustering of earthquakes (Dublanche et al., 2013; Cattania & Segall, 2021).
 607 The contribution of creep mediated stress transfers to temporal clustering might even
 608 be more important than static stress changes due to the breaking of asperities (Dublanche,
 609 2019). In fact, this means that both seismic and aseismic events can cluster in time, but
 610 that earthquake catalogs only capture the seismic signature of temporal clustering. Ef-
 611 fectively, these interacting stress fields result in a clock advance or delay in the cycle of
 612 the earthquake sources (*e.g.* Harris et al., 1995; Gombert et al., 1998) and thus in non-
 613 random earthquake sequences.

614 Figure 12 sketches different earthquake interaction scenarios explaining temporal
 615 clustering: in a locked fault Figure 12A, and with creep mediated stress transfers Fig-
 616 ure 12B. Note that remote creep acting on a sparse asperity population (Figure 12C) would
 617 produce Poissonian seismicity (*e.g.* Lohman & McGuire, 2007). Thus, areas of strong
 618 temporal clustering (see Figure 11) indicate faults with intrinsic properties: heteroge-
 619 neous rheology resulting in juxtaposed seismic and aseismic slip, and rough or densely
 620 fractured fault zone providing many seismogenic asperities. These properties enhance
 621 interaction-driven seismicity, that is, driven by the redistributed stresses of past events.
 622 However, the long time-scale behavior of clustered seismicity may be modulated by time-
 623 dependent remote forcing.

624 Where rheology transitions from brittle to ductile, for example at the base of the
 625 seismogenic zone, faults are likely to host both unstable, seismic slip and stable, aseis-
 626 mic slip (C. H. Scholz, 1998; Skarbak et al., 2012). Therefore, seismicity near the bot-
 627 tom of the seismogenic zone would be expected to display temporal clustering because,
 628 there, interacting asperities are likely to be embedded in a creeping fault (*cf.* Figure 12B,
 629 Dublanche et al., 2013). We investigated the relationship between temporal clustering
 630 and the proximity to the bottom of the seismogenic zone to elucidate the role of fault
 631 stability in our observations (*i.e.* scenario Figure 12A vs. 12B). The results, in Figure 13,
 632 indicate that, as expected, seismicity tends to get more time clustered as it gets closer
 633 to the brittle-ductile transition and that strong clustering almost always happens at the
 634 bottom of the seismogenic zone. Exceptions are at the western side of Lake Sapanca (Fig-
 635 ure 13B) where results might be biased due to the absence of significant seismicity at

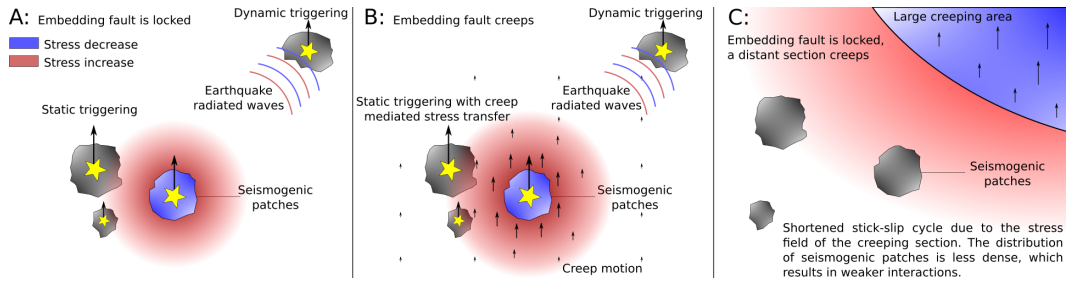


Figure 12. Sketch of different earthquake interaction scenarios. **A:** Seismogenic asperities embedded in a locked fault. **B:** Seismogenic asperities embedded in a creeping fault. In **A** and **B**, the color shows the stress change due to rupture of the seismogenic patch. The triggered ruptures occur with some delay. **C:** Seismogenic asperities embedded in a locked fault, but stressed by a remote creeping section of the fault. The asperities are not close enough to the creeping patch to strongly interact via static stress changes. The spatial configuration of asperities does not promote strong interactions.

636 depth, and along the Karadere segment (Figure 13F) where large source-receiver distances
 637 yield poor hypocentral depth resolution and thus low confidence results.

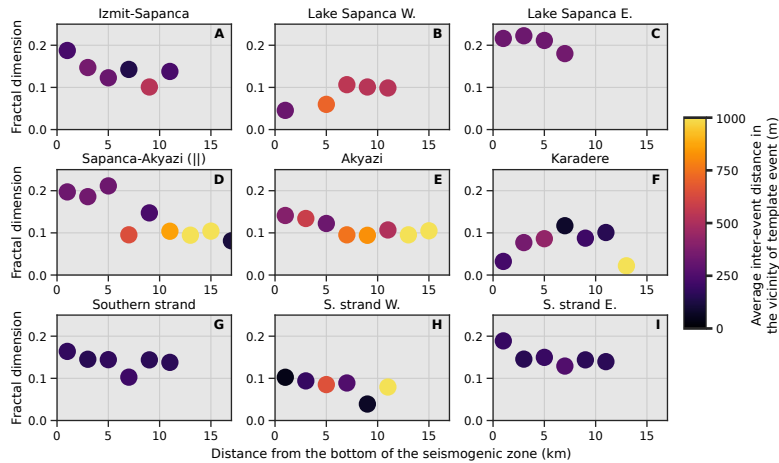


Figure 13. Clustering vs. depth vs. event density. Inside each region, templates are binned per distance from the bottom of the seismogenic zone and the fractal dimension is averaged among the 10% largest values, resulting in a "soft" maximum of each bin. The location of the bottom of the seismogenic zone is approximated by the depth of the locally deepest template. Dots are colored according to the average inter-event distance within the neighboring earthquake subcatalogs; this is a proxy for asperity density. Darker colors mean higher density. Strongest clustering tends to occur at the bottom of the seismogenic zone, *i.e.* at the transition zone between unstable (brittle) and stable (ductile) sliding.

638 We also investigated a possible correlation between the proximity to the brittle-
 639 ductile transition and the density of seismic sources, which could as well explain the in-
 640 crease in temporal clustering. We took the average inter-event distance within neigh-
 641 boring earthquake subcatalogs as a proxy for asperity density. We note that this measure
 642 of asperity density is imperfect because a single asperity can break repeatedly. The smaller

number of detected earthquakes along the southern strand might also be insufficient to compute a meaningful average inter-event distance. We do not observe a clear systematic increase in asperity density with decreasing distance from the bottom of the seismogenic zone, but the observational limits mentioned above prevent us from drawing definite conclusions. Figure 13 rather shows that both the proximity to the brittle-ductile transition and a large event density favor temporal clustering. Our observations therefore support that dense asperity populations along with creep mediated stress transfers do promote strong temporal clustering (*cf.* Figure 12B, Dublanche et al., 2013). Thus, this study suggests that faults at the eastern side of Lake Sapanca are in heterogeneous stability regimes allowing unstable (seismic) and stable (aseismic) slip.

4.4 Implications for the Lake Sapanca Step-Over

In summary, the Gutenberg-Richter b-values (see Section 4.2) and temporal clustering (see Section 4.3) point to the role of different rheological properties in producing earthquakes between the two sides of Lake Sapanca. At the western side, the shallow active sections seem incapable of producing strongly time clustered seismicity. At the eastern side, the depth distribution, the strong temporal clustering (Figure 11C), and the high b-values (Figure 10) suggest that thin along-dip fault sections slip in a mixed seismic and aseismic mode.

Heterogeneous faults near the brittle-ductile transition have stable and unstable sections (*e.g.* Collettini et al., 2011). Weakly unstable sections may produce transient episodes of slow slip (*e.g.* Bürgmann, 2018). The temporal distribution of earthquakes at the eastern Lake Sapanca (see Figure 8C) suggests that faults are slipping during intermittent episodes of deformation. Thus, the weakest sections of the faults at the eastern Lake Sapanca might be intermittently driven to slowly slip and, in turn, activate the seismogenic asperities (Skarbek et al., 2012; Cattania & Segall, 2021). The lack of seismicity along the up-dip sections suggests they are either fully locked or fully creeping, but there is no evidence for such a large creeping section in geodetic data (*e.g.* Aslan et al., 2019). Geologic data suggest that the so-called Sapanca Complex, constituted of weak serpentinites and strong metabasites (Akbarbayram et al., 2013, and references therein), might reach the southeastern side of Lake Sapanca at depth where we observe the highly clustered seismicity. Such lithology is consistent with the scenario of strong asperities embedded in a weak, stable fault. How much seismic moment is released through (partial) aseismic slip during these episodes of strong microseismicity remains an open question.

Whether these intermittent episodes of deformation are a permanent feature of Lake Sapanca or result from the mechanical changes that faults underwent because of co- and post-seismic stress changes is hard to elucidate entirely since our comparison with the past seismicity relies on unequal catalogs (see Section 3.1.3). However, we know from geodetic data that north-south extension around the Lake Sapanca step-over accelerated considerably following the Izmit earthquake (Ergintav et al., 2009; Hearn et al., 2009). Stress analyses have also shown that the NAFZ weakened after the Izmit-Düzce earthquake sequence (*e.g.* Pınar et al., 2010; Ickrath et al., 2015). Given that deformation in the step-over is faster than before the Izmit earthquake, (micro)seismicity should also be stronger. Early post Izmit-Düzce seismicity (before early 2001) is either lacking from the catalogs due to insufficient detection capability, or the increase of seismicity occurred later due to postseismic relaxation processes such as enhanced slip rates below seismogenic depths.

The postseismic response of at least two releasing step-overs of the NAFZ, Lake Sapanca and another one in the eastern Marmara Sea, has been shown to produce substantial north-south extension following the Izmit earthquake (Ergintav et al., 2009; Hearn et al., 2009). Ergintav et al. (2009) have shown that models of postseismic slip on the main fault do not account well for the north-south extension in these two step-overs, in particular after the first three years. We further compared these step-overs by extend-

696 ing our temporal clustering analysis further along the NAFZ and found that the east-
 697 ern Marmara Sea was also hosting clustered seismicity at the eastern termination of the
 698 Princes Islands segment (*cf.* Figure S6). Large earthquake location uncertainties pre-
 699 vented us from carrying the same detailed study but this section has been identified as
 700 an area of high b-value (Raub et al., 2017). We can hypothesize that Lake Sapanca and
 701 the eastern Marmara Sea behave similarly. In both cases, fault heterogeneities, and per-
 702 haps their stress history, could explain an hybrid seismic and aseismic slip regime (Collettini
 703 et al., 2011). As to how much slip is accommodated seismically vs. aseismically and whether
 704 the aseismic part is related to the deformation missing from the current models has to
 705 be addressed by the means of geodesy.

706 5 Summary and Concluding Remarks

707 We processed 1.5 years of continuous data collected during the DANA experiment
 708 (May 2012 - September 2013, see Data and Resources) with an automated earthquake
 709 detection and location method (Beaucé et al., 2019, and see Section 2) and produced an
 710 earthquake catalog with 31,329 events between 38.50°N-41.50°N and 28.00°E-32.00°E,
 711 with depths shallower than 20 km, and horizontal location uncertainty less than 15 km
 712 (see Section 3.1). We found that 14,655 detected events were induced or triggered by min-
 713 ing activity against 16,674 natural earthquakes, the latter mostly occurring outside of
 714 the North Anatolian Fault Zone itself. We focused our analysis on about 2,000 relocated
 715 earthquakes in the NAFZ and near the station array.

716 We analyzed the earthquake catalog to investigate collective properties of earth-
 717 quakes: the b-value of the Gutenberg-Richter law (see Section 3.2), which we related to
 718 the level of background stresses driving the ruptures (see Section 4.2), and the strength
 719 of temporal clustering (see Section 3.3), which we interpreted in terms of interacting stress
 720 fields and fault rheology (see Section 4.3). We showed that strongest temporal cluster-
 721 ing almost systematically occurred in the brittle-ductile transition zone, suggesting that
 722 a mixed seismic-aseismic slip regime enhances temporal clustering (see Section 4.3).

723 We found that the patterns of seismicity have changed durably after the Izmit-Düzce
 724 earthquake sequence (see Section 3.1.3). The region near the Akyazi fault, where the co-
 725 seismic displacement was noticeably low, was still one of the most active areas some thir-
 726 teen years later. This seismicity indicate a low b-value ($b \approx 0.8$, *cf.* Sections 3.2 and 4.2)
 727 and weak-to-moderate time clustering (see Sections 3.3 and 4.3), suggesting that the high
 728 residual stresses left by the absence of co-seismic release are driving the seismicity.

729 We also detected strong seismicity around Lake Sapanca. At the western side, we
 730 observed shallow (≈ 5 km, see Section 3.1.2) and weakly-to-moderately time clustered
 731 seismicity (see Section 3.3). Although it is occurring off the main fault, the depths and
 732 weak clustering are consistent with creep-driven seismicity (see Section 4.3, Figure 12C).
 733 The seismicity at the eastern side takes place in a narrow depth interval at the bottom
 734 of the seismogenic zone (≈ 10 -13 km depth, see Section 3.1.2), has a high b-value ($b \approx$
 735 1.1, see Section 3.2), and is strongly time clustered (see Section 3.3). We suggested that
 736 these are the characteristics of mixed seismic and aseismic slip on heterogeneous faults
 737 at the brittle-ductile transition. Such east-west differences over a short distance likely
 738 reflect the heterogeneous geology of the region (*e.g.* Akbayram et al., 2013). The pro-
 739 posed rheology of the faults at the eastern Lake Sapanca could indicate that these in-
 740 tersect the so-called Sapanca complex at depth, which is made of weak and strong ma-
 741 terials. The Lake Sapanca seismicity is a major feature of our earthquake catalog but
 742 might have been missed in the past due to insufficient detection capability (see Section 4.1).

743 The results of our study emphasize the important role of secondary structures in
 744 the late postseismic stage of the NAFZ, and possibly through the interseismic phase. The
 745 structural complexity of these structures appears in stark contrast to the relatively sim-
 746 ple co-seismic dynamics of the Izmit earthquake (*i.e.* rupture on almost straight and ver-
 747 tical fault segments Barka, 1999; Langridge et al., 2002). The north-south extension across
 748 the Lake Sapanca step-over accelerated following the Izmit earthquake (Ergintav et al.,

2009; Hearn et al., 2009), and we therefore question whether the proposed seismic-aseismic heterogeneous slip regime could be related to this deformation (see Section 4.4). The seismicity supports, but not prove, the possibility of slow slip in the step-over. We suggested that the releasing step-over in the Marmara Sea, with similar temporal clustering and accelerated extension following the Izmit earthquake, could behave analogously to the Lake Sapanca step-over. The present study does not provide the means to relate the observed surface deformation to slip on specific faults, but it does encourage the search for slow slip on normal faults in these step-overs. Finally, our study emphasizes that slip may not always happen in well separated seismic and aseismic sections but, instead, may happen over complex, intricate unstable and stable domains.

6 Data and Resources

The earthquake catalog is available at the Zenodo data set repository (DOI: 10.5281/zenodo.6362973). We used the version 1.0.1 of our BPMF Python package for earthquake detection and location, which is stored at <https://doi.org/10.5281/zenodo.6780316> (last accessed December 2021). The last version is maintained on Github at https://github.com/ebeauce/Seismic_BPMF.

The topographic data used for the maps were taken from the Shuttle Radar Topographic Mission (SRTM) 90-m database (<https://cgiarcsi.community/data/srtm-90m-digital-elevation-database-v4-1/>, last accessed December 2021). The maps were made with the Cartopy Python library (version 0.18.0, last accessed December 2021, Met Office, 2010 - 2015). The seismic data were recorded by the temporary array DANA (DANA, 2012, DOI: https://doi.org/10.7914/SN/YH_2012) and by the permanent KOERI stations (Kandilli Observatory And Earthquake Research Institute, Boğaziçi University, 1971, DOI: <https://doi.org/10.7914/SN/K0>).

Acknowledgements

This project has received funding from the European Research Council (ERC) under the European Union’s Horizon H2020 research and innovation program (grant agreement No 742335). E.B. was also supported by funds associated with Robert D. van der Hilst’s Schlumberger chair.

References

- 778
- 779 Akbayram, K., Okay, A. I., & Satir, M. (2013). Early cretaceous closure of the
780 intra-pontide ocean in western pontides (northwestern turkey). *Journal of Geo-*
781 *dynamics*, *65*, 38–55.
- 782 Aki, K. (1965). Maximum likelihood estimate of b in the formula $\log n = a - bm$ and
783 its confidence limits. *Bull. Earthq. Res. Inst., Tokyo Univ.*, *43*, 237–239.
- 784 Amelung, F., & King, G. (1997). Earthquake scaling laws for creeping and non-
785 creeping faults. *Geophysical research letters*, *24*(5), 507–510.
- 786 Amitrano, D. (2003). Brittle-ductile transition and associated seismicity: Exper-
787 imental and numerical studies and relationship with the b value. *Journal of*
788 *Geophysical Research: Solid Earth*, *108*(B1).
- 789 Aslan, G., Lasserre, C., Cakir, Z., Ergintav, S., Özarparci, S., Dogan, U., . . . Renard,
790 F. (2019). Shallow creep along the 1999 Izmit earthquake rupture (Turkey)
791 from GPS and high temporal resolution interferometric synthetic aperture
792 radar data (2011–2017). *Journal of Geophysical Research: Solid Earth*, *124*(2),
793 2218–2236.
- 794 Barka, A. (1999). The 17 august 1999 izmit earthquake. *Science*, *285*(5435), 1858–
795 1859.
- 796 Barka, A., Akyuz, H., Altunel, E., Sunal, G., Cakir, Z., Dikbas, A., . . . others
797 (2002). The surface rupture and slip distribution of the 17 august 1999 Izmit
798 earthquake (m 7.4), North Anatolian fault. *Bulletin of the Seismological Soci-*
799 *ety of America*, *92*(1), 43–60.
- 800 Bayrak, Y., & Öztürk, S. (2004). Spatial and temporal variations of the aftershock
801 sequences of the 1999 izmit and düzce earthquakes. *Earth, planets and space*,
802 *56*(10), 933–944.
- 803 Beaucé, E., Frank, W. B., Paul, A., Campillo, M., & van der Hilst, R. D. (2019).
804 Systematic detection of clustered seismicity beneath the Southwestern Alps.
805 *Journal of Geophysical Research: Solid Earth*, *124*(11), 11531–11548.
- 806 Beaucé, E., Frank, W. B., & Romanenko, A. (2018). Fast matched filter (FMF): An
807 efficient seismic matched-filter search for both CPU and GPU architectures.
808 *Seismological Research Letters*, *89*(1), 165–172.
- 809 Ben-Zion, Y., & Zaliapin, I. (2020). Localization and coalescence of seismicity before
810 large earthquakes. *Geophysical Journal International*, *223*(1), 561–583.
- 811 Bohnhoff, M., Bulut, F., Görgün, E., Milkereit, C., & Dresen, G. (2008). Seis-
812 motectonic setting at the north anatolian fault zone after the 1999 mw= 7.4
813 izmit earthquake based on high-resolution aftershock locations. *Advances in*
814 *Geosciences*, *14*, 85–92.
- 815 Bohnhoff, M., Grosse, H., & Dresen, G. (2006). Strain partitioning and stress rota-
816 tion at the North Anatolian fault zone from aftershock focal mechanisms of the
817 1999 Izmit m w= 7.4 earthquake. *Geophysical Journal International*, *166*(1),
818 373–385.
- 819 Bohnhoff, M., Ickrath, M., & Dresen, G. (2016). Seismicity distribution in con-
820 junction with spatiotemporal variations of coseismic slip and postseismic creep
821 along the combined 1999 izmit-düzce rupture. *Tectonophysics*, *686*, 132–145.
- 822 Bouchon, M., Bouin, M.-P., Karabulut, H., Toksöz, M. N., Dietrich, M., & Rosakis,
823 A. J. (2001). How fast is rupture during an earthquake? new insights from the
824 1999 Turkey earthquakes. *Geophysical Research Letters*, *28*(14), 2723–2726.
- 825 Bouchon, M., Karabulut, H., Aktar, M., Özalaybey, S., Schmittbuhl, J., & Bouin,
826 M.-P. (2011). Extended nucleation of the 1999 mw 7.6 Izmit earthquake.
827 *science*, *331*(6019), 877–880.
- 828 Brune, J. N. (1970). Tectonic stress and the spectra of seismic shear waves from
829 earthquakes. *Journal of geophysical research*, *75*(26), 4997–5009.
- 830 Bulut, F., Bohnhoff, M., Aktar, M., & Dresen, G. (2007). Characterization of
831 aftershock-fault plane orientations of the 1999 izmit (turkey) earthquake using
832 high-resolution aftershock locations. *Geophysical Research Letters*, *34*(20).

- 833 Bürgmann, R. (2018). The geophysics, geology and mechanics of slow fault slip.
834 *Earth and Planetary Science Letters*, *495*, 112–134.
- 835 Bürgmann, R., Ergintav, S., Segall, P., Hearn, E. H., McClusky, S., Reilinger, R. E.,
836 ... Zschau, J. (2002). Time-dependent distributed afterslip on and deep below
837 the izmit earthquake rupture. *Bulletin of the Seismological Society of America*,
838 *92*(1), 126–137.
- 839 Burridge, R., & Knopoff, L. (1967). Model and theoretical seismicity. *Bulletin of the*
840 *seismological society of america*, *57*(3), 341–371.
- 841 Cakir, Z., Chabalier, J.-B. d., Armijo, R., Meyer, B., Barka, A., & Peltzer, G.
842 (2003). Coseismic and early post-seismic slip associated with the 1999 izmit
843 earthquake (turkey), from sar interferometry and tectonic field observations.
844 *Geophysical Journal International*, *155*(1), 93–110.
- 845 Çakir, Z., Ergintav, S., Özener, H., Dogan, U., Akoglu, A. M., Meghraoui, M., &
846 Reilinger, R. (2012). Onset of aseismic creep on major strike-slip faults.
847 *Geology*, *40*(12), 1115–1118.
- 848 Cattania, C. (2019). Complex earthquake sequences on simple faults. *Geophysical*
849 *Research Letters*, *46*(17-18), 10384–10393.
- 850 Cattania, C., & Segall, P. (2021). Precursory slow slip and foreshocks on rough
851 faults. *Journal of Geophysical Research: Solid Earth*, *126*(4), e2020JB020430.
- 852 Collettini, C., Niemeijer, A., Viti, C., Smith, S. A., & Marone, C. (2011). Fault
853 structure, frictional properties and mixed-mode fault slip behavior. *Earth and*
854 *Planetary Science Letters*, *311*(3-4), 316–327.
- 855 Crampin, S., Evans, R., & Üçer, S. B. (1985). Analysis of records of local earth-
856 quakes: the turkish dilatancy projects (tdp1 and tdp2). *Geophysical Journal*
857 *International*, *83*(1), 1–16.
- 858 DANA . (2012). *Dense array for north anatolia*. International Federation of Digital
859 Seismograph Networks. Retrieved from [http://www.fdsn.org/doi/10.7914/](http://www.fdsn.org/doi/10.7914/SN/YH.2012)
860 [SN/YH.2012](http://www.fdsn.org/doi/10.7914/SN/YH.2012) doi: 10.7914/SN/YH.2012
- 861 Dolan, J. F., & Haravitch, B. D. (2014). How well do surface slip measurements
862 track slip at depth in large strike-slip earthquakes? the importance of fault
863 structural maturity in controlling on-fault slip versus off-fault surface deformation.
864 *Earth and Planetary Science Letters*, *388*, 38–47.
- 865 Dublanchet, P. (2019). Scaling and variability of interacting repeating earthquake
866 sequences controlled by asperity density. *Geophysical Research Letters*, *46*(21),
867 11950–11958.
- 868 Dublanchet, P., Bernard, P., & Favreau, P. (2013). Interactions and triggering in
869 a 3-d rate-and-state asperity model. *Journal of Geophysical Research: Solid*
870 *Earth*, *118*(5), 2225–2245.
- 871 Efron, B., & Tibshirani, R. (1986). Bootstrap methods for standard errors, confi-
872 dence intervals, and other measures of statistical accuracy. *Statistical science*,
873 54–75.
- 874 Ergintav, S., McClusky, S., Hearn, E., Reilinger, R., Cakmak, R., Herring, T., ...
875 Tari, E. (2009). Seven years of postseismic deformation following the 1999,
876 m= 7.4 and m= 7.2, izmit-düzce, turkey earthquake sequence. *Journal of*
877 *Geophysical Research: Solid Earth*, *114*(B7).
- 878 Fan, W., & Shearer, P. M. (2016). Local near instantaneously dynamically triggered
879 aftershocks of large earthquakes. *Science*, *353*(6304), 1133–1136.
- 880 Fischer, T., & Hainzl, S. (2021). The growth of earthquake clusters. *Frontiers in*
881 *Earth Science*, *9*, 79.
- 882 Frank, W., & Shapiro, N. (2014). Automatic detection of low-frequency earthquakes
883 (lfe) based on a beamformed network response. *Geophysical Journal Interna-*
884 *tional*, *197*(2), 1215–1223.
- 885 Frank, W. B., Shapiro, N. M., Husker, A. L., Kostoglodov, V., Gusev, A. A., &
886 Campillo, M. (2016). The evolving interaction of low-frequency earthquakes
887 during transient slip. *Science advances*, *2*(4), e1501616.

- 888 Gardner, J., & Knopoff, L. (1974). Is the sequence of earthquakes in Southern Cali-
 889 fornia, with aftershocks removed, Poissonian? *Bulletin of the Seismological So-*
 890 *ciety of America*, 64(5), 1363–1367.
- 891 Gibbons, S. J., & Ringdal, F. (2006). The detection of low magnitude seismic events
 892 using array-based waveform correlation. *Geophysical Journal International*,
 893 165(1), 149–166.
- 894 Gomberg, J., Beeler, N., Blanpied, M., & Bodin, P. (1998). Earthquake triggering
 895 by transient and static deformations. *Journal of Geophysical Research: Solid*
 896 *Earth*, 103(B10), 24411–24426.
- 897 Gutenberg, B., & Richter, C. (1941). *Seismicity of the earth* (Vol. 34). Geological
 898 Society of America.
- 899 Harris, R. A., Simpson, R. W., & Reasenber, P. A. (1995). Influence of static stress
 900 changes on earthquake locations in southern california. *Nature*, 375(6528),
 901 221–224.
- 902 Hearn, E., McClusky, S., Ergintav, S., & Reilinger, R. (2009). Izmit earthquake
 903 postseismic deformation and dynamics of the north anatolian fault zone. *Jour-*
 904 *nal of Geophysical Research: Solid Earth*, 114(B8).
- 905 Honda, R., & Aoi, S. (2009). Array back-projection imaging of the 2007 Niigataken
 906 Chuetsu-oki earthquake striking the world’s largest nuclear power plant. *Bul-*
 907 *letin of the Seismological Society of America*, 99(1), 141–147.
- 908 Hussain, E., Wright, T. J., Walters, R. J., Bekaert, D., Hooper, A., & Houseman,
 909 G. A. (2016). Geodetic observations of postseismic creep in the decade af-
 910 ter the 1999 Izmit earthquake, Turkey: Implications for a shallow slip deficit.
 911 *Journal of Geophysical Research: Solid Earth*, 121(4), 2980–3001.
- 912 Ickrath, M., Bohnhoff, M., Dresen, G., Martinez-Garzon, P., Bulut, F., Kwiatek, G.,
 913 & Germer, O. (2015). Detailed analysis of spatiotemporal variations of the
 914 stress field orientation along the izmit-düzce rupture in nw turkey from inver-
 915 sion of first-motion polarity data. *Geophysical Journal International*, 202(3),
 916 2120–2132.
- 917 Ishii, M., Shearer, P. M., Houston, H., & Vidale, J. E. (2005). Extent, duration and
 918 speed of the 2004 Sumatra–Andaman earthquake imaged by the Hi-Net array.
 919 *Nature*, 435(7044), 933.
- 920 Ito, A., Uçer, B., Barış, Ş., Nakamura, A., Honkura, Y., Kono, T., ... Işikara, A. M.
 921 (2002). Aftershock activity of the 1999 izmit, turkey, earthquake revealed
 922 from microearthquake observations. *Bulletin of the Seismological Society of*
 923 *America*, 92(1), 418–427.
- 924 Kahraman, M., Cornwell, D. G., Thompson, D. A., Rost, S., Houseman, G. A.,
 925 Türkelli, N., ... Gülen, L. (2015, Nov). Crustal-scale shear zones and hetero-
 926 geneous structure beneath the North Anatolian Fault Zone, Turkey, revealed
 927 by a high-density seismometer array. *Earth Planet. Sci. Lett.*, 430, 129–139.
 928 doi: 10.1016/j.epsl.2015.08.014
- 929 Kandilli Observatory And Earthquake Research Institute, Boğaziçi University.
 930 (1971). *Bogazici university kandilli observatory and earthquake research in-*
 931 *stitute*. International Federation of Digital Seismograph Networks. Retrieved
 932 from <http://www.fdsn.org/doi/10.7914/SN/KO> doi: 10.7914/SN/KO
- 933 Karabulut, H., Schmittbuhl, J., Özalaybey, S., Lengline, O., Kömeç-Mutlu, A., Du-
 934 rand, V., ... Bouin, M. (2011). Evolution of the seismicity in the eastern
 935 Marmara Sea a decade before and after the 17 August 1999 Izmit earthquake.
 936 *Tectonophysics*, 510(1-2), 17–27.
- 937 Karahan, A. E., Berckhemer, H., & Baier, B. (2001). Crustal structure at the west-
 938 ern end of the North Anatolian Fault Zone from deep seismic sounding.
- 939 King, G., & Cocco, M. (2001). Fault interaction by elastic stress changes: New clues
 940 from earthquake sequences. In *Advances in geophysics* (Vol. 44, pp. 1–VIII).
 941 Elsevier.
- 942 Langridge, R., Stenner, H. D., Fumal, T., Christofferson, S., Rockwell, T., Hartleb,

- 943 R., ... Barka, A. (2002). Geometry, slip distribution, and kinematics of surface
 944 rupture on the sakarya fault segment during the 17 august 1999 izmit, turkey,
 945 earthquake. *Bulletin of the Seismological Society of America*, *92*(1), 107–125.
- 946 Lee, H.-K., & Swarcz, H. P. (1995). Fractal clustering of fault activity in californi-
 947 a. *Geology*, *23*(4), 377–380.
- 948 Le Pichon, X., & Angelier, J. (1979). The hellenic arc and trench system: a key to
 949 the neotectonic evolution of the eastern mediterranean area. *Tectonophysics*,
 950 *60*(1-2), 1–42.
- 951 Lohman, R., & McGuire, J. (2007). Earthquake swarms driven by aseismic creep
 952 in the salton trough, california. *Journal of Geophysical Research: Solid Earth*,
 953 *112*(B4).
- 954 Lomax, A., Michelini, A., Curtis, A., & Meyers, R. (2009). Earthquake location,
 955 direct, global-search methods. *Encyclopedia of complexity and systems science*,
 956 *5*, 2449–2473.
- 957 Lomax, A., Virieux, J., Volant, P., & Berge-Thierry, C. (2000). Probabilistic earth-
 958 quake location in 3D and layered models. In *Advances in seismic event location*
 959 (pp. 101–134). Springer.
- 960 Lovell, J., Crampin, S., Evans, R., & Üçer, S. B. (1987). Microearthquakes in the
 961 tdp swarm, turkey: clustering in space and time. *Geophysical Journal Interna-*
 962 *tional*, *91*(2), 313–330.
- 963 Lowen, S. B., & Teich, M. C. (2005). *Fractal-based point processes* (Vol. 366). John
 964 Wiley & Sons.
- 965 Marsan, D., & Lengline, O. (2008). Extending earthquakes' reach through cascading.
 966 *Science*, *319*(5866), 1076–1079.
- 967 McClusky, S., Balassanian, S., Barka, A., Demir, C., Ergintav, S., Georgiev, I., ...
 968 others (2000). Global positioning system constraints on plate kinematics and
 969 dynamics in the eastern mediterranean and caucasus. *Journal of Geophysical*
 970 *Research: Solid Earth*, *105*(B3), 5695–5719.
- 971 Meade, B. J., Hager, B. H., McClusky, S. C., Reilinger, R. E., Ergintav, S., Lenk,
 972 O., ... Ozener, H. (2002). Estimates of seismic potential in the marmara
 973 sea region from block models of secular deformation constrained by global
 974 positioning system measurements. *Bulletin of the Seismological Society of*
 975 *America*, *92*(1), 208–215.
- 976 Met Office. (2010 - 2015). Cartopy: a cartographic python library with a matplotlib
 977 interface [Computer software manual]. Exeter, Devon. Retrieved from [http://](http://scitools.org.uk/cartopy)
 978 scitools.org.uk/cartopy
- 979 Moreau, L., Stehly, L., Boué, P., Lu, Y., Larose, E., & Campillo, M. (2017). Improv-
 980 ing ambient noise correlation functions with an SVD-based Wiener filter. *Geo-*
 981 *physical Journal International*, *211*(1), 418–426.
- 982 Mori, J., & Abercrombie, R. E. (1997). Depth dependence of earthquake frequency-
 983 magnitude distributions in california: Implications for rupture initiation. *Jour-*
 984 *nal of Geophysical Research: Solid Earth*, *102*(B7), 15081–15090.
- 985 Ozalaybey, S., Ergin, M., Aktar, M., Tapirdamaz, C., Biçmen, F., & Yörük, A.
 986 (2002). The 1999 izmit earthquake sequence in turkey: seismological and
 987 tectonic aspects. *Bulletin of the Seismological Society of America*, *92*(1),
 988 376–386.
- 989 Papaleo, E., Cornwell, D., & Rawlinson, N. (2018). Constraints on North Anatolian
 990 Fault Zone width in the crust and upper mantle from S wave teleseismic to-
 991 mography. *Journal of Geophysical Research: Solid Earth*, *123*(4), 2908–2922.
- 992 Parsons, T., Toda, S., Stein, R. S., Barka, A., & Dieterich, J. H. (2000). Height-
 993 ened odds of large earthquakes near istanbul: An interaction-based probability
 994 calculation. *Science*, *288*(5466), 661–665.
- 995 Perfettini, H., & Avouac, J.-P. (2004). Postseismic relaxation driven by brittle
 996 creep: A possible mechanism to reconcile geodetic measurements and the decay
 997 rate of aftershocks, application to the chi-chi earthquake, taiwan. *Journal of*

- 998 *Geophysical Research: Solid Earth*, 109(B2).
- 999 Pınar, A., Üçer, S., Honkura, Y., Sezgin, N., Ito, A., Barış, Ş., ... Horiuchi, S.
- 1000 (2010). Spatial variation of the stress field along the fault rupture zone of the
- 1001 1999 Izmit earthquake. *Earth, planets and space*, 62(3), 237–256.
- 1002 Poupinet, G., Ellsworth, W., & Frechet, J. (1984). Monitoring velocity variations
- 1003 in the crust using earthquake doublets: An application to the calaveras fault,
- 1004 california. *Journal of Geophysical Research: Solid Earth*, 89(B7), 5719–5731.
- 1005 Poyraz, S. A., Teoman, M. U., Türkelli, N., Kahraman, M., Cambaz, D., Mutlu, A.,
- 1006 ... others (2015). New constraints on micro-seismicity and stress state in the
- 1007 western part of the North Anatolian Fault Zone: Observations from a dense
- 1008 seismic array. *Tectonophysics*, 656, 190–201.
- 1009 Raub, C., Martínez-Garzón, P., Kwiatek, G., Bohnhoff, M., & Dresen, G. (2017).
- 1010 Variations of seismic b-value at different stages of the seismic cycle along the
- 1011 north anatolian fault zone in northwestern turkey. *Tectonophysics*, 712, 232–
- 1012 248.
- 1013 Reilinger, R., Ergintav, S., Bürgmann, R., McClusky, S., Lenk, O., Barka, A., ...
- 1014 others (2000). Coseismic and postseismic fault slip for the 17 august 1999, m=
- 1015 7.5, izmit, turkey earthquake. *Science*, 289(5484), 1519–1524.
- 1016 Reilinger, R., McClusky, S., Vernant, P., Lawrence, S., Ergintav, S., Cakmak, R.,
- 1017 ... others (2006). GPS constraints on continental deformation in the Africa-
- 1018 Arabia-Eurasia continental collision zone and implications for the dynamics of
- 1019 plate interactions. *Journal of Geophysical Research: Solid Earth*, 111(B5).
- 1020 Ross, Z. E., Trugman, D. T., Hauksson, E., & Shearer, P. M. (2019). Searching for
- 1021 hidden earthquakes in Southern California. *Science*, eaaw6888.
- 1022 Scholz, C. (1968). Microfractures, aftershocks, and seismicity. *Bulletin of the Seis-*
- 1023 *mological Society of America*, 58(3), 1117–1130.
- 1024 Scholz, C. H. (1968). The frequency-magnitude relation of microfracturing in rock
- 1025 and its relation to earthquakes. *Bulletin of the seismological society of Amer-*
- 1026 *ica*, 58(1), 399–415.
- 1027 Scholz, C. H. (1998). Earthquakes and friction laws. *Nature*, 391(6662), 37–42.
- 1028 Scholz, C. H. (2015). On the stress dependence of the earthquake b value. *Geophys-*
- 1029 *ical Research Letters*, 42(5), 1399–1402.
- 1030 Shelly, D. R., Beroza, G. C., & Ide, S. (2007). Non-volcanic tremor and low-
- 1031 frequency earthquake swarms. *Nature*, 446(7133), 305.
- 1032 Skarbak, R. M., Rempel, A. W., & Schmidt, D. A. (2012). Geologic heterogeneity
- 1033 can produce aseismic slip transients. *Geophysical Research Letters*, 39(21).
- 1034 Smalley Jr, R. F., Chatelain, J.-L., Turcotte, D. L., & Prévot, R. (1987). A fractal
- 1035 approach to the clustering of earthquakes: applications to the seismicity of
- 1036 the new hebrides. *Bulletin of the Seismological Society of America*, 77(4),
- 1037 1368–1381.
- 1038 Stein, R. S., Barka, A. A., & Dieterich, J. H. (1997). Progressive failure on the
- 1039 North Anatolian fault since 1939 by earthquake stress triggering. *Geophysical*
- 1040 *Journal International*, 128(3), 594–604.
- 1041 Taylor, G., Rost, S., Houseman, G. A., & Hillers, G. (2019). Near-surface structure
- 1042 of the North Anatolian Fault zone from Rayleigh and Love wave tomography
- 1043 using ambient seismic noise. *Solid Earth*, 10(2), 363–378.
- 1044 Toksoz, M., Reilinger, R., Doll, C., Barka, A., & Yalcin, N. (1999). Izmit (Turkey)
- 1045 earthquake of 17 August 1999: first report. *Seismological Research Letters*,
- 1046 70(6), 669–679.
- 1047 Toksöz, M., Shakal, A., & Michael, A. (1979). Space-time migration of earthquakes
- 1048 along the North Anatolian fault zone and seismic gaps. *Pure and Applied Geo-*
- 1049 *physics*, 117(6), 1258–1270.
- 1050 Tormann, T., Wiemer, S., Metzger, S., Michael, A., & Hardebeck, J. L. (2013). Size
- 1051 distribution of parkfield’s microearthquakes reflects changes in surface creep
- 1052 rate. *Geophysical Journal International*, 193(3), 1474–1478.

- 1053 Trugman, D. T., & Shearer, P. M. (2017). GrowClust: A hierarchical clustering
1054 algorithm for relative earthquake relocation, with application to the Spanish
1055 Springs and Sheldon, Nevada, earthquake sequences. *Seismological Research
1056 Letters*, *88*(2A), 379–391.
- 1057 Utkucu, M., Nalbant, S. S., McCloskey, J., Steacy, S., & Alptekin, Ö. (2003). Slip
1058 distribution and stress changes associated with the 1999 november 12, düzce
1059 (turkey) earthquake (mw= 7.1). *Geophysical Journal International*, *153*(1),
1060 229–241.
- 1061 Utsu, T. (1966). A statistical significance test of the difference in b-value between
1062 two earthquake groups. *Journal of Physics of the Earth*, *14*(2), 37–40.
- 1063 Utsu, T., Ogata, Y., et al. (1995). The centenary of the omori formula for a decay
1064 law of aftershock activity. *Journal of Physics of the Earth*, *43*(1), 1–33.
- 1065 Waldhauser, F., & Ellsworth, W. L. (2000). A double-difference earthquake location
1066 algorithm: Method and application to the northern hayward fault, california.
1067 *Bulletin of the Seismological Society of America*, *90*(6), 1353–1368.
- 1068 Walker, K. T., Ishii, M., & Shearer, P. M. (2005). Rupture details of the 28 March
1069 2005 Sumatra Mw 8.6 earthquake imaged with teleseismic P waves. *Geophysical
1070 Research Letters*, *32*(24).
- 1071 White, M. C., Fang, H., Nakata, N., & Ben-Zion, Y. (2020). PyKonal: A Python
1072 Package for Solving the Eikonal Equation in Spherical and Cartesian Coordi-
1073 nates Using the Fast Marching Method. *Seismological Research Letters*, *91*(4),
1074 2378–2389.
- 1075 Wiemer, S., & Katsumata, K. (1999). Spatial variability of seismicity parameters
1076 in aftershock zones. *Journal of Geophysical Research: Solid Earth*, *104*(B6),
1077 13135–13151.
- 1078 Wiemer, S., & Wyss, M. (1997). Mapping the frequency-magnitude distribution
1079 in asperities: An improved technique to calculate recurrence times? *Journal of
1080 Geophysical Research: Solid Earth*, *102*(B7), 15115–15128.
- 1081 Zhu, W., & Beroza, G. C. (2019). PhaseNet: a deep-neural-network-based seismic
1082 arrival-time picking method. *Geophysical Journal International*, *216*(1), 261–
1083 273.